UNIVERSITÀ DEGLI STUDI DI PADOVA

Dipartimento di Fisica e Astronomia "Galileo Galilei"

Master Degree in Physics

Final Dissertation

Phenomenology of Pseudo Nambu-Goldstone Dark Matter

Thesis supervisor

Dr. Ennio Salvioni

Candidate

Riccardo Masarotti

Academic Year 2021/2022

Contents

A map to this thesis

The microscopic nature of dark matter (DM) is one of the key open problems in fundamental physics. Over the last few years, the theoretical proposal that DM may be a pseudo Nambu-Goldstone boson (pNGB) particle has risen to prominence, because it explains by elegant symmetry arguments the lack of signals in direct detection experiments. This thesis discusses several aspects of pNGB DM.

After a general introduction to particle DM in Chapter 1, the most salient phenomenological features of pNGB DM are presented in Chapter 2. Chapters 3 and 4 review the existing literature on pNGB DM models, considering first extended composite Higgs scenarios where the Higgs and DM arise as "sibling" pNGBs (Chapter 3), then discussing simple scalar extensions of the Standard Model that give rise to pNGB DM (Chapter 4). Notice that a review of pNGB DM physics has not appeared to date in the literature.

Chapter 5 contains the main original results of this thesis: it focuses on the prospects to probe pNGB DM at a future muon collider (MC), through its pair-production in vector boson fusion (VBF) mediated by an off-shell Higgs. This process yields large missing mass, plus a muon and an anti-muon at large rapidities. To record such muons, a dedicated forward detector would need to be installed at the MC. Here a first estimate of the required coverage and resolution is attempted, based on the pNGB DM signal as well as the related cases of VBF production through the off-shell renormalizable Higgs portal, and on-shell Higgs decay to invisible particles. Conclusions are drawn in Chapter 6.

Chapter 1

Introduction to dark matter

When it comes to the matter component of the energy balance of the Universe, the Standard Model (SM) particles only provide about 15%, while dark matter (DM) contributes the dominant 85%. Nowadays we are able to obtain information about DM from measurements on a variety of scales, but at the beginning of its history, hints of its existence could only be acquired from observations of galaxies. It is interesting to briefly trace back the historical path of evidences for DM.

1.1 Evidences for dark matter

The understanding of gravitation theory was revolutionized in 1915 by Einstein's General Relativity theory, which became an essential tool to investigate the Universe. In the following decades, the combination of theoretical and technological progress would lead to the birth of cosmology. The dark matter hypothesis was first proposed by astronomers in the 1930s. They were helped by new technological developments allowing to make better astronomical observations at larger scales with good resolutions. The first mentions of dark matter came by astronomer Jan Oort in 1932 [1], who worked on measuring the motion of the brightest stars in the Milky Way: his results suggested a "missing mass" problem, namely, the inferred mass appeared to be larger than the directly observed one. One year later, work by Fritz Zwicky provided a significant hint for the existence of dark matter [2]. The Coma Cluster was his object of investigation, where he measured the average velocities of visible galaxies: the key consideration came exploiting the virial theorem, which allowed him to estimate the mass of the entire cluster. A disagreement appeared when the resulting estimate of the cluster mass was compared to the estimate of the visible mass: the former was found to be approximately 400 times greater than the latter, a hint of missing matter in the system. Even though Zwicky's estimate was, in hindsight, too large by an order of magnitude, he did correctly conclude that most of the matter in the cluster was dark.

The next significant step would need to wait about 40 years, until the work of Vera Rubin. The object of her study was the motion of stars within spiral galaxies, aiming to produce galactic rotation curves, which show the orbital velocity of stars as function of their distance from the galaxy center. Rubin's studies on the subject began in 1970 and culminated in a landmark paper published ten years later [3], see Fig. 1.1. To qualitatively understand Rubin's results, we estimate the stars' circular velocities by writing down the equation of motion $F = ma$, namely

$$\frac{G_N m M(r)}{r^2} = m\frac{v_c^2(r)}{r} \quad \Longrightarrow \quad v_c(r) = \sqrt{\frac{G_N M(r)}{r}} \tag{1.1}$$

according to Newtonian gravity, where $M(r)$ is the mass enclosed within radius r. At distances larger than the radius of the galactic disk, $r > R_{\text{disk}}$, from Gauss' law the enclosed mass should remain constant, leaving us with $v_c(r) \propto r^{-1/2}$. This is known as the "Keplerian" decrease, referring to the observed behavior of the orbital velocities of the planets around the Sun. Rubin's results, which covered 21 different spiral galaxies, showed however that most galaxies *did not* exhibit the expected

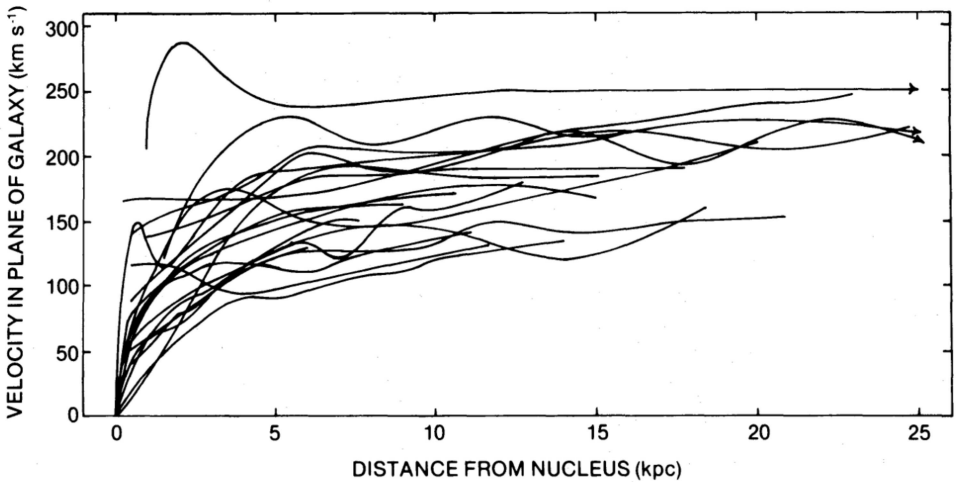

Figure 1.1: Galactic rotation curves of the 21 spiral galaxies from [3]. Notice that most curves flatten out at large radius.

decrease of v_c at large radius, but rather had rotation curves that flattened out outside the disk. This has been further confirmed by radio astronomy measurements of the 21-cm atomic hydrogen line, which also have a long history [4] and have made it possible to extend the rotation curves to larger distances from the galactic center.

From Eq. (1.1), the flattening of the rotation curves implies $M(r) \propto r$, suggesting the presence of a dark component of matter that extends far beyond the stellar disk. Assuming the dark matter to be distributed in a spherically symmetric halo, one finds that its mass density distribution should obey $\rho(r) \propto M(r)/r^3 \sim r^{-2}$. How large is the halo? Taking as example the Milky Way, which has a disk of size $R_{\rm disk} \sim 10$ kpc, we can estimate [5] the size of the dark matter halo from

$$M_{\rm halo} \sim 4\pi \int_0^{R_{\rm halo}} dr\, r^2 \rho(r) = 4\pi R_{\rm halo} \rho_0 r_0^2 \,, \tag{1.2}$$

with $\rho(r) = \rho_0(r_0^2/r^2)$, where the 0 subscript denotes local quantities. Stellar kinematics determine the distance of the Sun from the galactic center as $r_0 \sim 8.5$ kpc, whereas $\rho_0 \sim 0.3$ GeV/cm^3 and $M_{\rm halo} \sim 10^{12} M_\odot$. Plugging in these numbers gives $R_{\rm halo} \sim 200$ kpc. While this estimate is very rough, it does tell us that the dark matter halo is far bigger than the visible disk.

We continue by mentioning other evidences for dark matter. The Cosmic Microwave Background (CMB) provides strong support for the dark matter hypothesis, and also allows to determine with high precision the energy densities of the different components of the Universe. The CMB spectrum is known to correspond to a blackbody with $T_0 \simeq 2.73$ K (henceforth, the 0 subscript denotes quantities today) and to be approximately isotropic, with small temperature fluctuations of size $\delta T/T \approx 10^{-5}$. Measurements of the CMB anisotropies give us the opportunity to look back at the Universe at the time of recombination, $T \sim 0.3$ eV. The strategy is to expand them in spherical harmonics on the solid angle and obtain the power spectrum, which is the principal observable of interest. The most recent results have been provided by the Planck Collaboration in 2018 [6]: in figure 1.2 the power spectrum of temperature fluctuations is reported as a function of the multipole moment ℓ. Dots indicate the experimental values, while the light blue line indicates the best-fit prediction of the ΛCDM standard model of cosmology, which includes cold dark matter (CDM) as well as a cosmological constant (Λ). The CMB power spectrum is very sensitive to the amount of dark matter present in the Universe [7]. The current best values of the matter energy densities are

$$\begin{cases} \Omega_b^0 h^2 = 0.02237 \pm 0.00015 \,, \\ \Omega_c^0 h^2 = 0.1200 \pm 0.0012 \,, \end{cases} \tag{1.3}$$

as obtained by Planck (c indicates CDM, and $h \equiv H_0/(100\ {\rm km\,s^{-1}\,Mpc^{-1}})$.

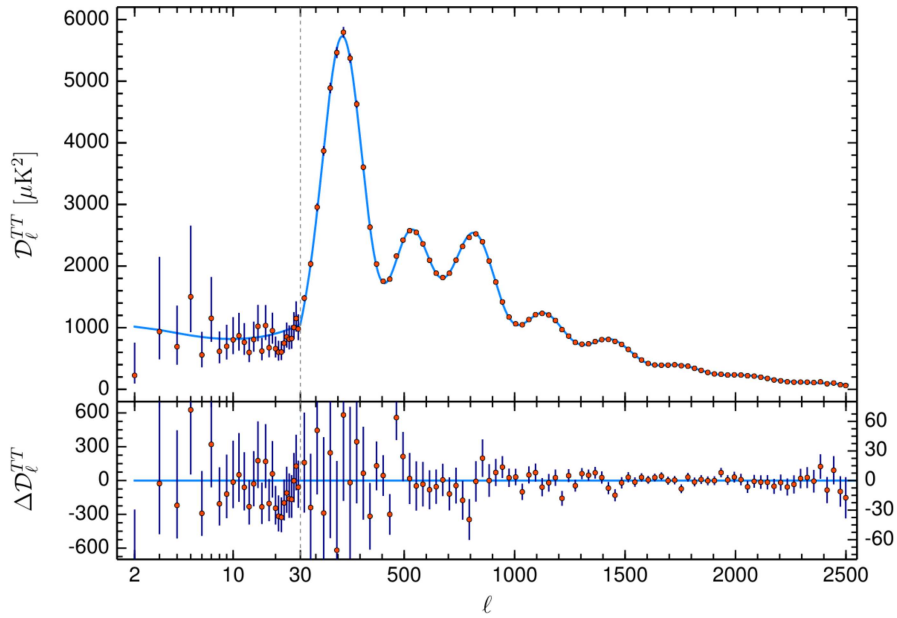

Figure 1.2: Temperature power spectrum from [6]. The best-fit prediction of the ΛCDM model is represented by the light blue line, while dots correspond to experimental data. The lower panel shows the residuals with respect to the fiducial model.

A further indication of dark matter's existence arises from observations of the Large Scale Structure (LSS) of the Universe today. Similarly to the CMB discussion outlined above, one introduces the power spectrum of matter density fluctuations at a certain time. The starting point is represented by the density fluctuation function and its Fourier transform,

$$\delta(\vec{x},t) = \frac{\rho(\vec{x},t) - \bar{\rho}(t)}{\bar{\rho}(t)} = \int \frac{d^3k}{(2\pi)^3} e^{-i\vec{k}\cdot\vec{x}} \tilde{\delta}(\vec{k},t)\,, \tag{1.4}$$

for which one computes the correlator

$$\left\langle \tilde{\delta}(\vec{k})\tilde{\delta}^*(\vec{k}') \right\rangle = (2\pi)^3 \delta^3(\vec{k}-\vec{k}') P(k)\,, \tag{1.5}$$

where $P(k)$ is the power spectrum and δ^3 is the three-dimensional Dirac delta. Important qualitative differences exist with respect to the CMB, in particular because fluctuations in the Universe today are large on small scales, but LSS observations also have strong sensitivity to the presence of dark matter [8, 9].

Observations of galaxy clusters furnish additional indications in favor of dark matter. Measurements of the X-ray emission from the ionized gas forming the intracluster medium allow astronomers to obtain screenshots of the gas temperature T and density n profiles. Under the assumption of hydrostatic equilibrium for a spherically symmetric system, one finds for the mass enclosed within radius r the result [10]

$$M(r) = -\frac{r\,kT}{G_N \mu m_p} \left[\frac{\mathrm{d}\log n}{\mathrm{d}\log r} + \frac{\mathrm{d}\log T}{\mathrm{d}\log r} \right]\,, \tag{1.6}$$

where μm_p is the mean molecular weight and k is the Boltzmann constant. This represents the gravitational mass, thus it also includes the non-luminous component. The comparison with measurements of the luminous mass again points to the presence of dark matter in the system.

Additional evidence for dark matter comes from gravitational lensing, namely the bending of light rays due to the spacetime's alteration by a massive object, such as for example a galaxy cluster. We can distinguish between strong lensing, where the effect has great strength and leads to multiple images of the same distant object, and weak lensing, where smaller effects are present and measured on a

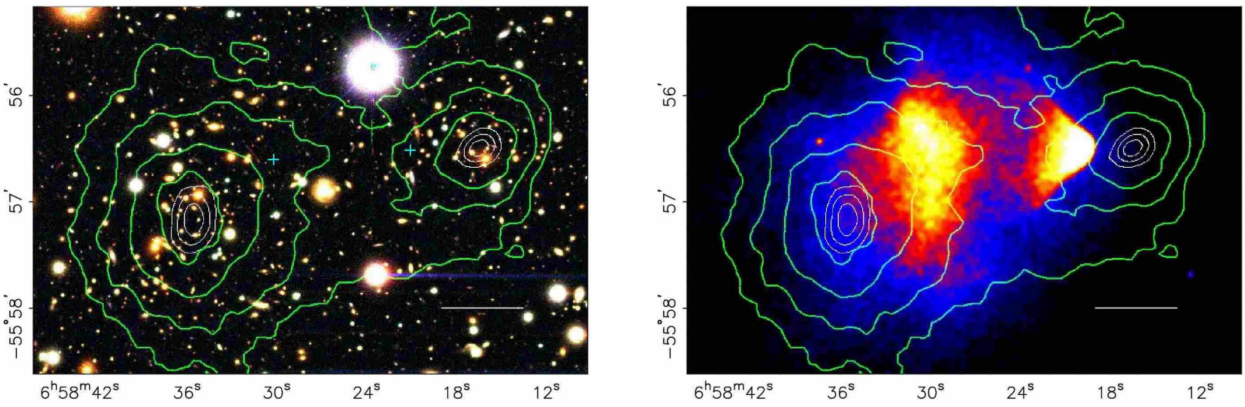

Figure 1.3: Merging cluster 1E0657-558. In both figures, green lines are directly related to the gravitational mass density: from the outermost contour to the innermost, there is an equal increase at each step. The left picture is an optical image of part of the cluster, while the right one is an X-ray image displaying the gas distribution, to be compared with the distribution of the mass. Figures taken from [14].

statistical basis. Lensing measurements both in the weak [11] and strong [12] regimes are consistent with the presence of dark matter halos. For more details, we refer the reader to [13].

Finally, we mention the evidence in favor of dark matter coming from the *Bullet Cluster* (1E0657-558), a merger of two galaxy clusters [14]. It has two galaxy concentrations 0.72 Mpc far one from the other, and the two cores are supposed to have passed through each other around 100 My ago. During such a merging event, different interactions are expected among the individual components. The gaseous components of the two clusters, which constitute most of the baryonic matter present in the system, are significantly slowed down by electromagnetic interactions, as shown by X-rays measurements. On the other hand, stars are collisionless and therefore lay "far ahead" of the gas, as observed with optical measurements, see Fig. 1.3. Finally, and crucially, weak lensing measurements allow to determine the spatial distribution of the total gravitational mass. This is found to be clearly shifted from the gas, and coinciding to first approximation with the positions of the visible stars. This is precisely what is expected if most of the mass is concentrated in two clumps of collisionless dark matter, which have not been appreciably slowed down in the collision. Vice versa, in absence of dark matter we would expect to find a matching between the gravitational potential as determined by lensing and the distribution of the gas.

The above discussion provides convincing support for the existence of dark matter, which is assumed in the rest of this thesis. Nevertheless, it is worth mentioning that alternative theories exist, which attempt to explain the above phenomena by modifying gravity on galactic scales: Modified Newtonian Dynamics (MOND) [15], and its relativistic version Tensor-Vector-Scalar gravity (TeVeS) [16]. It is fair to say that, so far, these alternative proposals have not been able to match the extensive set of observations we have just reviewed.

1.2 Known properties of dark matter

Although the previous section gives compelling arguments in favor of the existence of dark matter, its particle nature, origin and possible interactions with ordinary matter are still unknown. Nevertheless, we have been able to understand some general properties of dark matter through experiments and observations carried out during 90 years of history, considering Zwicky's work as the starting point.

As we already mentioned, we know that dark matter was present at the time of recombination, due to its effects on the CMB, and we know its important effects today. Hence, dark matter should be a stable particle, or at least should have a lifetime longer than the age of the Universe, $\simeq 14$ Gy $= 4 \cdot 10^{17}$ s.

Furthermore, dark matter should be non-baryonic: an important argument supporting this comes from Big Bang Nucleosynthesis (BBN), which studies the formation of nuclei during the thermal history of

the Universe. Heavier elements were formed by a "series" of nuclear processes, starting with

$$\begin{aligned} \mathrm{p} + \mathrm{n} &\to \mathrm{d} + \dots \\ \mathrm{p} + \mathrm{d} &\to {}^3\mathrm{He} + \dots \\ \mathrm{d} + \mathrm{d} &\to {}^4\mathrm{He} + \dots \end{aligned}$$

where d represents the deuterium. The key point is that the theoretical predictions for several of these reactions depend strongly on the baryon density. Hence, comparison with experimental measurements of light element abundances allows to determine $\Omega_b^0 h^2 \approx 0.022$. The total matter density $\Omega_m^0 h^2 \approx 0.14$ as obtained from the CMB then indicates that most of matter should be non-baryonic. The BBN determination of $\Omega_b^0 h^2$ is also in striking agreement with the CMB value in Eq. (1.3).

Concerning the *mass* of dark matter particles, model-independent bounds can be obtained by requiring that dark matter form halos (see, for instance, [5]). The bound depends on whether dark matter is assumed to be a boson or a fermion. In the bosonic case, identical particles can be packed together in the same point of the phase space. For very small masses the occupation number can be so high that dark matter can be effectively treated as a classical field, and a lower bound on the mass can be derived by imposing the uncertainty principle to halos: $\Delta x\, \Delta p \gtrsim \hbar$, where $\Delta x \approx 2R_{\rm halo}$ and $\Delta p \approx m_{\rm DM} v$. The strongest constraint comes from dwarf galaxies, for which $v \sim 10^{-4}$ and $2R_{\rm halo} \sim$ kpc, resulting in

$$m_{\rm DM,\,boson} \gtrsim 10^{-22}\ \mathrm{eV}\,. \tag{1.7}$$

By contrast, in the fermionic case we need to apply the Pauli exclusion principle [17], leading to

$$M_{\rm halo} = m_{\rm DM} V \int d^3p\, f(p) \lesssim m_{\rm DM} V \int d^3p \sim m_{\rm DM} R_{\rm halo}^3 (m_{\rm DM} v)^3\,, \tag{1.8}$$

where f is the fermionic density distribution. Plugging in the expression of the virial velocity from Eq. (1.1) gives

$$m_{\rm DM,\,fermion} \gtrsim \left(G_N^3 M_{\rm halo} R_{\rm halo}^3\right)^{-1/8} \sim O(10)\ \mathrm{eV}\,, \tag{1.9}$$

where we have used the values of $M_{\rm halo}$ and $R_{\rm halo}$ estimated above for the Milky Way. Refinements of this argument lead to a somewhat stronger requirement,

$$m_{\rm DM,\,fermion} \gtrsim 0.7\ \mathrm{keV}\,. \tag{1.10}$$

We see that this bound is far more stringent than the bosonic one.

Next, we turn to the interactions of dark matter. All the evidences obtained thus far relies on gravity, and establishing that dark matter has non-gravitational interactions may be viewed as the holy grail of dark matter searches. Dark matter particles should also have zero electromagnetic charge, to excellent approximation. While the assumption of ΛCDM is that dark matter is collisionless, experimental constraints only exclude rather large values for the (velocity-independent) self-interaction cross section: observations of the Bullet Cluster [18] give the bound $\sigma_{\rm self}/m_{\rm DM} \lesssim \mathrm{cm}^2\mathrm{g}^{-1}$.

Another important piece of information comes from the study of structure formation, which indicates that dark matter should be *cold*, i.e., it should be characterized by a small velocity dispersion in the early Universe. *Hot* dark matter leads to a different evolution of cosmological perturbations, in particular suppressing structure on small scales. This is also one reason why the Standard Model neutrinos are excluded as candidates for dark matter, because they decoupled from the thermal bath while relativistic.

1.3 Thermal dark matter and WIMPs

In light of the above discussion, the well-known observation that the Standard Model of particle physics does not contain a candidate for dark matter becomes clear. We are thus pushed to physics Beyond the Standard Model (BSM). A compelling option is provided by thermal scenarios, where the dark

matter particle was in equilibrium with the thermal bath in the early Universe. This is attractive, because it renders the mechanism setting the dark matter relic density insensitive to cosmological initial conditions. In this thesis, we focus on thermal dark matter candidates. It is important to keep in mind, however, that non-thermal scenarios are also very interesting and extensively studied.

The simplest class of thermal scenarios, and the one on which we focus here, is when the dark matter is initially in equilibrium with the Standard Model plasma, through a process $\chi\chi \leftrightarrow$ SM SM. In a nutshell, the picture is as follows. At $T \gg m_\chi$ both the forward and backward processes are fast, so that the χ density follows the equilibrium distribution. Eventually, as the temperature drops below m_χ , it becomes increasingly more difficult for a χ particle to find a partner to annihilate with, until the (comoving) number density of dark matter particles "freezes out", namely it becomes constant. The temperature (or equivalently time) at which the freezeout happens, $T_{\rm FO}$, can be inferred by comparing the annihilation rate with the Hubble expansion rate H: the approximate condition is

$$\Gamma_{\rm ann} = n_{\chi,\,\rm eq}\langle\sigma v\rangle \simeq H\,, \tag{1.11}$$

where $n_{\chi,\,\rm eq}$ is the equilibrium dark matter number density, while $\langle\sigma v\rangle$ is the thermal average of the cross section for $\chi\chi \to$ SM SM annihilation times velocity. Equation (1.11) marks the chemical decoupling between dark matter and the bath. The picture we have just described corresponds to freeze out of dark matter in the non-relativistic regime, $T_{\rm FO} \ll m_\chi$, which gives a cold relic as demanded by structure formation.

1.3.1 The freeze-out mechanism

While estimates based on the simplified condition (1.11) are very useful, to gain a deeper understanding we need to derive the Boltzmann equation that governs the evolution of the dark matter number density. We follow the discussions in [19–23]. The starting point is

$$L[f] = C[f]\,, \tag{1.12}$$

where $f(\vec{x},\vec{p},t)$ is the phase space distribution of dark matter particles. The left-hand side stands for the *Liouville operator* and the right-hand one for the *collision operator*. The general covariant form of the Liouville operator is

$$L[f] = P^\mu \frac{\partial f}{\partial x^\mu} - \Gamma^\mu_{\alpha\beta} P^\alpha P^\beta \frac{\partial f}{\partial P^\mu}\,, \tag{1.13}$$

where $\Gamma^\mu_{\alpha\beta}$ are the Christoffel symbols associated to the Friedmann-Lemaître-Robertson-Walker metric for an isotropic and homogeneous Universe, $ds^2 = dt^2 - a^2(t)\left(dr^2 + r^2 d\Omega\right)$. We can then write $f = f(E,t)$. Using $P^\mu = (E, p^i/a)$ and $\Gamma^0_{ij} = \delta_{ij}\, a\,\dot{a}$ (dots denote time derivatives), we obtain

$$L[f] = E\frac{\partial f}{\partial t} - Hp^2\frac{\partial f}{\partial E} \tag{1.14}$$

where $H(t) \equiv \dot{a}(t)/a(t)$. Recalling how the number density is defined in terms of the phase space distribution,

$$n(t) \equiv \frac{g}{(2\pi)^3}\int d^3p f(E,t)\,, \tag{1.15}$$

where g is the number of degrees of freedom, we can rewrite the left-hand side of the Boltzmann equation as

$$\frac{g}{(2\pi)^3}\int d^3p \frac{L[f]}{E} = \frac{dn}{dt} + 3Hn\,, \tag{1.16}$$

upon use of $\partial f/\partial E = (E/p)\,\partial f/\partial p$ and integration by parts. We thus arrive at

$$\frac{dn}{dt} + 3Hn = \frac{g}{(2\pi)^3}\int d^3p \frac{C[f]}{E}\,. \tag{1.17}$$

Suppose for a moment that we have no collisions. Then the number density should simply be diluted by the expansion of the volume of the Universe, $n \propto a^{-3}$. This is indeed what one finds from Eq. (1.17) for $C[f] = 0$.

The collision operator, on the other hand, specifies how the distribution is changing due to interactions. We are interested in $2 \to 2$ scatterings: for a $1 + 2 \leftrightarrow 3 + 4$ process, the collision term for the first particle is given by

$$\frac{g_1}{(2\pi)^3}\int d^3p_1 \frac{C[f_1]}{E_1} = -\int d\Pi_1 d\Pi_2 d\Pi_3 d\Pi_4 (2\pi)^4 \delta^4(p_1 + p_2 - p_3 - p_4) \times \left[f_1 f_2 (1 \pm f_3)(1 \pm f_4) \left|\mathscr{M}_{12\to 34}\right|^2 - f_3 f_4 (1 \pm f_1)(1 \pm f_2) \left|\mathscr{M}_{34\to 12}\right|^2\right] \quad (1.18)$$

where the $+$ sign applies to bosons and the $-$ to fermions, and the amplitudes are averaged over initial and final spins. We have defined

$$d\Pi_i = \frac{g_i}{(2\pi)^3}\frac{d^3p_i}{2E_i}\,. \quad (1.19)$$

We can make progress by means of several simplifying assumptions. First, we use Maxwell distributions instead of Fermi-Dirac or Bose-Einstein ones, assuming that for each species $T_i \ll E_i$ (and neglecting chemical potentials for simplicity). This yields $(1 \pm f_i) \simeq 1$ and $f_i^{\rm eq} = \exp(-E_i/T)$. Next, we make use of the relation between cross section and squared matrix element,

$$\int d\Pi_k d\Pi_l (2\pi)^4 \left|\mathscr{M}_{ij\to kl}\right|^2 \delta^4(p_i + p_j - p_k - p_l) = 4\,\sigma_{ij\to kl}\left[\left(p_i \cdot p_j\right)^2 - m_i^2 m_j^2\right]^{\frac{1}{2}} = 4E_i E_j\,\sigma_{ij\to kl}(v_{\rm M\o l})_{ij} \quad (1.20)$$

where $(v_{\rm M\o l})_{ij} \equiv \left[\left(p_i \cdot p_j\right)^2 - m_i^2 m_j^2\right]^{\frac{1}{2}}/(E_i E_j)$ is the Møller velocity, allowing us to rewrite

$$\frac{g_1}{(2\pi)^3}\int d^3p_1 \frac{C[f_1]}{E_1} = -\int (\sigma v_{\rm M\o l})_{12}\frac{g_1 d^3p_1}{(2\pi)^3} f_1 \frac{g_2 d^3p_2}{(2\pi)^3} f_2 + \int (\sigma v_{\rm M\o l})_{34}\frac{g_3 d^3p_3}{(2\pi)^3} f_3 \frac{g_4 d^3p_4}{(2\pi)^3} f_4\,. \quad (1.21)$$

Now since $(\sigma v_{\rm M\o l})_{12}$ is slowly varying in the integral over $dn_1 dn_2$, we can pull its thermally averaged value out of the integral, arriving at

$$\frac{dn_1}{dt} + 3Hn_1 = -\langle\sigma v_{\rm M\o l}\rangle_{12} n_1 n_2 + \langle\sigma v_{\rm M\o l}\rangle_{34} n_3 n_4\,, \quad (1.22)$$

where

$$\langle\sigma v_{\rm M\o l}\rangle_{12} \equiv \frac{\int dn_1^{\rm eq} dn_2^{\rm eq} (\sigma v_{\rm M\o l})_{12}}{\int dn_1^{\rm eq} dn_2^{\rm eq}}\,. \quad (1.23)$$

To proceed further we specialize to the case where 1 and 2 are identical DM particles χ, while 3 and 4 are Standard Model particles in thermal equilibrium with the photon bath, giving $n_{3,4} = n_{3,4}^{\rm eq}$. Finally, the principle of detailed balance (which rests on T, or equivalently CP, invariance) dictates that when the DM is in equilibrium with the bath, $\langle\sigma v_{\rm M\o l}\rangle_{12} n_{\chi,\,\rm eq}^2 = \langle\sigma v_{\rm M\o l}\rangle_{34} n_3^{\rm eq} n_4^{\rm eq}$. Then we have

$$\frac{dn_\chi}{dt} + 3Hn_\chi = -\langle\sigma v_{\rm M\o l}\rangle(n_\chi^2 - n_{\chi,\,\rm eq}^2)\,, \quad (1.24)$$

where $\langle\sigma v_{\rm M\o l}\rangle = \langle\sigma v_{\rm M\o l}\rangle_{12}$. This is the Boltzmann equation that describes the evolution of the DM number density under the expansion of the Universe and the annihilation process $\chi\chi \leftrightarrow$ SM SM.

We can make one further step by taking as convenient variable the comoving number density (also known as *yield*)

$$Y_\chi \equiv \frac{n_\chi}{s}\,, \quad (1.25)$$

where taking the ratio to the total entropy density s factors out the expansion of the Universe. Recalling that $s \propto a^{-3}$, we write

$$\frac{dY_\chi}{dt} = \frac{1}{s}\left(\frac{dn_\chi}{dt} + 3Hn_\chi\right) = -\langle\sigma v_{\rm M\o l}\rangle s\left(Y_\chi^2 - Y_{\chi,\,\rm eq}^2\right)\,. \quad (1.26)$$

Furthermore it is convenient to switch to the dimensionless variable $x \equiv m_\chi/T$, by means of the relation $g_{*s}T^3a^3 = \text{const}$, which leads to $da/a = \left(1 + \frac{1}{3}\frac{d\log g_{*s}}{d\log T}\right) dx/x$ and ultimately to

$$\frac{dY_\chi}{dx} = -\langle\sigma v\rangle \frac{s}{\tilde{H}x}\left(Y_\chi^2 - Y_{\chi,\,\mathrm{eq}}^2\right), \tag{1.27}$$

where $\tilde{H} \equiv H/\left(1 + \frac{1}{3}\frac{d\log g_{*s}}{d\log T}\right)$ and v indicates $v_{\mathrm{M\o l}}$, as it will be done for simplicity in the rest of this work. It is often reasonable to set $\tilde{H} \simeq H$, neglecting the temperature dependence of the total number of degrees of freedom. The equation (1.27) has no closed-form solution in general, so one needs to proceed with semi-analytical or numerical approaches. Recall that the general idea was that if $\Gamma_{\mathrm{ann}} \gg H$, then the equilibrium is kept by efficient annihilation processes, on the other hand for $\Gamma_{\mathrm{ann}} \ll H$ the dark matter is decoupled from the thermal bath. In terms of the comoving number density and the x variable, we have

$$Y_\chi(x \lesssim x_f) \simeq Y_{\chi,\,\mathrm{eq}}(x)\,, \qquad Y_\chi(x \gtrsim x_f) \simeq Y_{\chi,\,\mathrm{eq}}(x_f)\,, \tag{1.28}$$

where $x_f \equiv m_\chi/T_{\mathrm{FO}}$.

1.3.2 The WIMP miracle

We now focus on the cold relic scenario, where $x_f \gtrsim 3$. We can make explicit the dependencies on x, namely $H(x) = H(x=1)x^{-2}$ and $s(x) = s(x=1)x^{-3}$. Furthermore, we can parametrize the thermally averaged cross section $\langle\sigma v\rangle$ as follows. We have $\sigma v \propto v^{2n}$, where $n = 0$ for s-wave, $n = 1$ for p-wave, etc., and $\langle v^2\rangle \sim T$, hence $\langle\sigma v\rangle \propto T^n$. Thus, we write

$$\langle\sigma v\rangle \equiv \bar{\sigma}\, x^{-n} \tag{1.29}$$

and Eq. (1.27) can be cast in the form

$$\frac{dY_\chi}{dx} = -\frac{\lambda}{x^{n+2}}\left(Y_\chi^2 - Y_{\chi,\,\mathrm{eq}}^2\right) \qquad \text{where} \qquad \lambda \equiv \frac{\bar{\sigma}s(x=1)}{H(x=1)}\,, \quad Y_{\chi,\,\mathrm{eq}} = \frac{45}{4\pi^4}\sqrt{\frac{\pi}{2}}\frac{g_\chi}{g_{*s}}x^{3/2}e^{-x}\,. \tag{1.30}$$

The approximate solution can be obtained by rewriting the equation in terms of the variable $\Delta \equiv Y_\chi - Y_{\chi,\,\mathrm{eq}}$. By simple algebra one finds

$$\frac{d\Delta}{dx} = -\frac{dY_{\chi,\,\mathrm{eq}}}{dx} - \lambda x^{-n-2}\Delta\left(2Y_{\chi,\,\mathrm{eq}} + \Delta\right). \tag{1.31}$$

At early times, before freeze-out, we expect to be very close to equilibrium, so it is reasonable to impose $d\Delta/dx = 0$ with Δ small, which leads to

$$\Delta \simeq -\frac{x^{n+2}}{\lambda}\frac{dY_{\chi,\,\mathrm{eq}}/dx}{2Y_{\chi,\,\mathrm{eq}} + \Delta} \simeq \frac{x^{n+2}}{2\lambda}\,. \qquad (x < x_f) \tag{1.32}$$

On the other hand, at late times after the freeze-out we expect $Y_{\chi,\,\mathrm{eq}}$ to be irrelevant with respect to Y_χ, thus

$$\frac{d\Delta}{dx} \simeq -\frac{\lambda}{x^{n+2}}\Delta^2\,, \qquad (x > x_f) \tag{1.33}$$

which can be integrated between $x = x_f$ and $x = \infty$ (which means today) to give

$$Y_{\chi,\,0} = \frac{n+1}{\lambda}\, x_f^{n+1} \tag{1.34}$$

where we have used the fact that $\Delta_f \gg \Delta_\infty$, as one sees by estimating the former using Eq. (1.32) and $x_f \gg 1$.

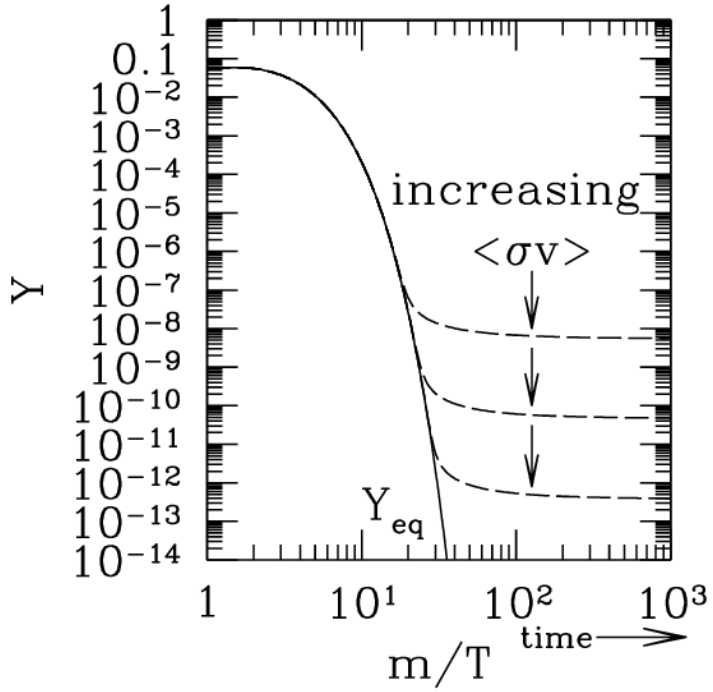

Figure 1.4: Typical behavior of the comoving number density as function of $x = m_\chi/T$. The solid line shows the equilibrium distribution $Y_{\chi,\,\mathrm{eq}}$, while the dashed lines give Y_χ after the freeze-out. The effect of increasing the annihilation cross section is highlighted. Figure taken from [21].

We now need to estimate x_f. To do so, notice that x_f is the time when Δ becomes of order $Y_{\chi,\,\mathrm{eq}}$: defining the freeze-out condition as $\Delta(x_f) = cY_{\chi,\,\mathrm{eq}}(x_f)$ with $c \sim O(1)$, the early time solution (1.32) becomes $\Delta(x_f) \simeq x_f^{n+2}/[\lambda(2+c)]$ and equating these two expressions leads to

$$x_f \simeq \log\left[\lambda(2+c)cA\right] - (n+1/2)\log\left\{\log\left[\lambda(2+c)cA\right]\right\}\,, \tag{1.35}$$

where $A \equiv \frac{45}{4\pi^4}\sqrt{\frac{\pi}{2}}\frac{g_\chi}{g_{*s}}$. The most accurate fit to the numerical solutions is obtained setting $(2+c)c = n+1$. The exact numerical solution can be observed in Fig. 1.4. The behavior fully confirms our discussion: at high temperature, Y_χ tracks $Y_{\chi,\,\mathrm{eq}}$. As the temperature decreases and the evolution reaches the freeze-out time, when the Hubble expansion rate and dark matter annihilation cross section become comparable, Y_χ departs from $Y_{\chi,\,\mathrm{eq}}$, with the former remaining approximately constant until today. We see that a larger annihilation cross section is associated to a smaller relic density. This is expected, because stronger interactions are able to preserve the equilibrium for a longer time.

Another, simpler way to reach similar results is to apply the instantaneous freeze-out condition (1.11), leading to

$$x_f^{\frac{1}{2}-n}e^{-x_f} \simeq \left(\frac{8\pi^5 g_*}{90}\right)^{1/2}\frac{1}{g_\chi m_\chi M_{\mathrm{Pl}}\bar{\sigma}}\,, \tag{1.36}$$

solved by

$$x_f \simeq \log\left[\lambda A\right] - (n-1/2)\log\left\{\log\left[\lambda A\right]\right\}\,, \tag{1.37}$$

which for $n = 0$ is nearly identical to (1.35) with $(2+c)c = n+1$.

In view of these results, we are finally ready to introduce the so-called WIMP miracle, where WIMP stands for Weakly Interacting Massive Particle. Using the above calculations and writing $\langle\sigma v\rangle = \pi\alpha^2/m_\chi^2$, one finds for weak scale mass $m_\chi \sim 100$ GeV and weak interaction strength $\alpha \sim 0.01$ that $x_f \simeq 25$, and for the DM relic abundance

$$\Omega_\chi^0 h^2 = \frac{\rho_\chi^0}{\rho_{\mathrm{cr}}/h^2} = \frac{m_\chi Y_{\chi,\,\mathrm{eq}}(x_f)s_0}{\rho_{\mathrm{cr}}/h^2} \sim 0.1\left(\frac{0.01}{\alpha}\right)^2\left(\frac{m_\chi}{100\ \mathrm{GeV}}\right)^2\,. \tag{1.38}$$

Thus, for a WIMP the freeze-out mechanism naturally yields a DM relic abundance in the correct ballpark. This coincidence, known as "WIMP miracle", actually allows for a wider mass range of thermal candidates (roughly 1 GeV to 10 TeV), provided the interaction strength is suitably adjusted. Owing to the simplicity and robustness of thermal freeze-out, and to important links with other open questions in particle physics – most importantly, the hierarchy problem of the weak scale – WIMPs have received enormous attention as DM candidates. A wide-ranging program of searches has been established in the past decades, and we now turn to a very brief review of these efforts.

1.4 WIMP dark matter searches

Experimental searches for WIMP dark matter can be divided into three main groups, which are distinguished by their working principles:

- Direct detection;
- Indirect detection;
- Collider searches.

Direct detection experiments aim at observing elastic scattering processes $\chi + \mathrm{SM} \to \chi + \mathrm{SM}$. With indirect detection, one looks for DM annihilation processes to Standard Model particles, focusing on regions of the Universe with high expected dark matter density. Collider searches hope to observe production of DM in the high-energy scattering of Standard Model particles. In the remainder of this section we discuss these three strategies in turn, limiting ourselves to a qualitative introduction. Nonetheless, Fig. 1.5 is important, in that it summarizes the current status (November 2022) of searches for nuclear recoils. As we discuss in Chapter 2, this status provides an important phenomenological motivation for pNGB dark matter.

Direct detection

We follow [24, 25], where the concepts presented here are treated in greater detail. Direct detection experiments seek to reveal the elastic scattering of dark matter on ordinary matter on Earth. Since DM cannot be directly observed, the signal is (in the mass range discussed in this thesis, $m_{\mathrm{DM}} \gtrsim 10$ GeV) a nuclear recoil "apparently coming out from nowhere". Historically, the first suggestion of direct detection experiments came from Goodman and Witten in 1985 [26]. Direct detection experiments can be divided into several classes. In general, the detected signals can be represented by scintillation light, collected by means of photomultipliers; electric charge, when ionization occurs and the free electrons are collected applying an electric field; and heat or phonons, respectively through thermal and athermal sensors in materials. Furthermore, several types of targets are used, including for instance cryogenic crystal detectors and liquid noble gases.

In recent years and for the foreseeable future, the leading sensitivity comes from Xenon-based experiments. Let us mention the most important actors. The XENON project at LNGS started its activities in 2006 and has been since then upgraded with progressive target mass increases, from XENON10 with $O(10)$ kg of liquid Xe, to XENON1T with $O(1)$ ton, which released its final nuclear recoil results in 2018 [27]. The next phase, XENONnT, is expected to provide its first results very soon. The Particle and Astrophysical Xenon Detector, or PandaX, based at the CJPL, has released in 2021 results from its 4T phase, yielding slightly stronger limits compared to XENON1T [28]. Finally, the LUX-ZEPLIN (LZ) project at SURF, a merger of the previous LUX and ZEPLIN collaborations, has provided in the Summer of 2022 the strongest limits to date [29].

Indirect detection

A nice description of the recent status of indirect detection experiments is provided in [30], to which the interested reader is referred. Historically, the first suggestion of looking for annihilation products came in 1978 [31] and has developed into a wide field with a very large number of experiments and

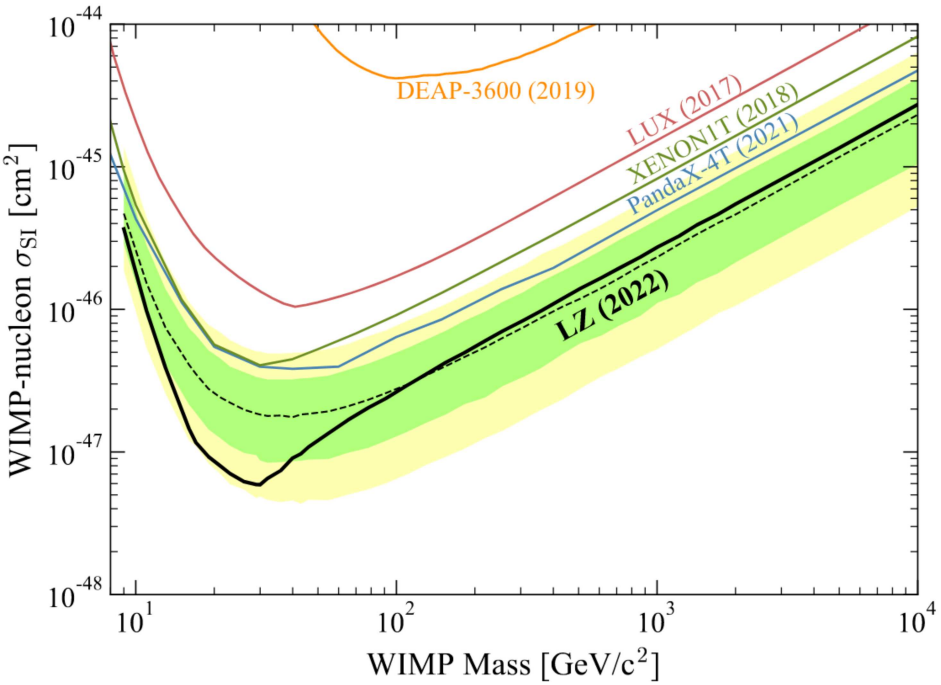

Figure 1.5: Most significant upper bounds on the spin-independent cross section between WIMPs and nucleons. Figure taken from the paper reporting the best current bound, obtained by the LZ collaboration [29].

collaborations. Indirect searches target regions where the dark matter density is expected to be enhanced, such as the center of the Milky Way or dwarf galaxies. Compared with direct detection experiments, indirect searches face a different set of issues in order to extract reliable results: in fact the "target" region is now not under control, and one also has to consider the significant distance that Standard Model products of DM annihilation travel to reach our telescopes. During their flight, two main effects can be expected: firstly, it is not guaranteed that all of them are stable, thus they might decay before reaching the Earth; secondly, charged particles are affected by the presence of magnetic fields in the Universe. Currently, some of the most reliable bounds on DM annihilation (in the mass range of interest for this thesis) come from gamma ray searches, notably at the Fermi Gamma-Ray Telescope [32], while in the near future the Cherenkov Telescope Array is expected to extend the sensitivity to the thermal target cross section $\langle \sigma v \rangle_{\text{canonical}} \simeq 2 \times 10^{-26} \text{cm}^3\,\text{s}^{-1}$ to considerably higher DM masses and into the multi-TeV region [33].

Collider searches

The third and last class of experiments we consider, are those that aim to produce DM particles at accelerators. For the WIMP mass range we are interested in, the most important constraints have been obtained at LEP, TeVatron, and the LHC. Since collider production will be extensively discussed in this thesis for the pNGB DM scenario, here we only mention a few general aspects; see [34–36] for extended treatments.

At hadron colliders such as the LHC, DM particles are expected to be produced in pairs and to leave undetected, leading to missing transverse momentum. In this sense, it is important to keep in mind that collider experiments alone cannot establish a discovery of DM, but rather of some particle with a sufficiently long lifetime to escape the detector. Examples of searches include "mono-X" processes, where X stands for a hadronic jet, a photon, a W, Z or Higgs boson, and so on. Another important class of signatures, which will be discussed in Chapter 2, involves the Higgs boson, either through its decay to a DM pair or through its off-shell mediation of DM pair production. In less minimal models where mediators accompany the DM, a much wider set of signals becomes possible, now not necessarily involving invisible final states. Discussing these would take us too far. Instead, it is now time to introduce the main subject of this thesis: pNGB dark matter.

Chapter 2

pNGB dark matter phenomenology

We now introduce pNGB DM, which is a scalar particle ϕ, singlet under the SM gauge symmetries, characterized by the following minimal Lagrangian:

$$\mathscr{L}_{\rm derivative} = \mathscr{L}_{\rm SM} + \frac{1}{2}\partial_\mu\phi\partial^\mu\phi - \frac{1}{2}m_\phi^2\phi^2 + \frac{c_d}{2f^2}\partial_\mu(|H|^2)\,\partial^\mu(\phi^2)\,, \tag{2.1}$$

where the dimension-6 operator coupling the DM to the SM goes under the name of *derivative* Higgs portal. Although one could set $c_d = 1$, it is sometimes useful to retain the coefficient explicitly, when comparing to other higher-dimensional operators that may be generated as well.

Phenomenologically, the key feature of this simple setup is that, due to proportionality of the portal strength to the momentum transfer q^2, one has s-wave annihilation to SM particles (where $q^2 \sim m_\phi^2$), but extremely suppressed scattering on nuclei (where $q^2 \sim m_\phi^2 v_{\rm DM}^2$ with $v_{\rm DM} \sim 10^{-3}$). Thus, pNGB DM is a WIMP DM candidate that does not suffer from any tension with the null results of direct detection searches.

The derivative portal arises naturally as the consequence of shift symmetries. Theoretically, two classes of concrete models motivate pNGB DM. The first class consists of composite Higgs models with an extended global symmetry breaking pattern, where both the Higgs and DM effectively arise as "sibling" pseudo-Goldstone modes. These models provide a unified solution to the electroweak hierarchy and DM problems, and f can be identified with the decay constant of the Goldstone bosons, in analogy with f_π for low-energy QCD. The second class consists of extensions of the SM by a complex scalar field S, whose angular mode is identified with the pNGB DM. A suitably-chosen term that breaks explicitly the U(1) symmetry, $\mu^2(S^2 + \text{h.c.})$, is included to generate a mass for ϕ. At energies below the radial mode mass, one obtains the structure in Eq. (2.1). In this class of models, the Higgs is an elementary field and the hierarchy problem is not addressed.

In this chapter we present the main phenomenological features of pNGB DM and the derivative Higgs portal, postponing to Chapters 3 and 4 a review of concrete models. As an important term of comparison, we will also discuss the *renormalizable* (or *marginal*) Higgs portal DM [37–39],

$$\mathscr{L}_{\rm marginal} = \mathscr{L}_{\rm SM} + \frac{1}{2}\partial_\mu\phi\partial^\mu\phi - \frac{1}{2}M_\phi^2\phi^2 - \frac{\lambda}{2}|H|^2\phi^2\,, \tag{2.2}$$

which is extremely well-studied and, as we are going to discuss, is now mostly excluded for masses $m_\phi \lesssim 3$ TeV, where $m_\phi^2 = M_\phi^2 + \lambda v^2/2$.

2.1 Derivative Higgs portal

The essential aspects of the derivative Higgs portal, which appears in Eq. (2.1), can be summarized as follows.

2.1.1 Theoretical predictions

DM annihilation to SM particles

Recalling Eq. (1.27), to calculate the freezeout of pNGB DM we need the expression of $\langle\sigma v\rangle$ for the derivative Higgs portal. Several final states are important, including WW, ZZ, hh, and $f\bar{f}$.

As an example, we focus on annihilation to a fermion-antifermion pair, which is mediated by s-channel exchange of a Higgs boson. The amplitude reads

$$\mathscr{M} = \bar{u}(p_3)v(p_4)\left(\frac{iy_f v}{\sqrt{2}}\right)\left(\frac{1}{s-m_h^2}\right)\left(\frac{c_d}{f^2}s\right). \tag{2.3}$$

From the latter we get the squared amplitude summed over final state spins and averaged over initial state spins,

$$\left|\overline{\mathscr{M}}\right|^2 = 2m_f^2(s-4m_f^2)\left(\frac{1}{s-m_h^2}\right)^2\left(\frac{c_d}{f^2}s\right)^2. \tag{2.4}$$

In the center of mass frame,

$$\frac{\mathrm{d}\sigma_{\mathrm{CM}}}{\mathrm{d}\Omega} = \frac{1}{16\pi^2}\frac{1}{sv_{\mathrm{rel}}}\frac{|\vec{p}_f|}{\sqrt{s}}\left|\overline{\mathscr{M}}\right|^2 \tag{2.5}$$

with $|\vec{p}_f| = \frac{1}{2}(s-4m_f^2)^{\frac{1}{2}}$, thus integrating over angles

$$\sigma_{\mathrm{CM}}v_{\mathrm{rel}} = \frac{m_f^2}{4\pi}\left(1-\frac{4m_f^2}{s}\right)^{\frac{3}{2}}\frac{1}{(s-m_h^2)^2}\left(\frac{c_d}{f^2}s\right)^2. \tag{2.6}$$

Notice that in the center of mass frame, $v_{\mathrm{M\o l}} = v_{\mathrm{rel}}$. The thermal average over the cross section is written in general as [19]

$$\langle\sigma_{\mathrm{CM}}v_{\mathrm{rel}}\rangle(T) = \frac{1}{16m_\phi^4TK_2^2(m_\phi/T)}\int_{4m_\phi^2}^{+\infty}ds\,s\sqrt{s-4m_\phi^2}\,K_1(\sqrt{s}/T)\sigma_{\mathrm{CM}}v_{\mathrm{rel}}(s)\,, \tag{2.7}$$

with K_i modified Bessel functions of the second kind. To extract the dominant s-wave piece, the cross section is expanded around the threshold $s = 4m_\phi^2$ and the truncated expansion at leading order is inserted into the integral. Thus, the thermally averaged cross section is well approximated by

$$\langle\sigma_{\mathrm{CM}}v_{\mathrm{rel}}\rangle(T) \simeq \sigma_{\mathrm{CM}}v_{\mathrm{rel}}(s=4m_\phi^2) = \frac{c_d^2m_f^2}{4\pi f^4}\left(1-\frac{m_f^2}{m_\phi^2}\right)^{\frac{3}{2}}\left(1-\frac{m_h^2}{4m_\phi^2}\right)^{-2}. \tag{2.8}$$

Notice the proportionality to m_f^2, which implies preferred annihilation to the heaviest SM fermion that is kinematically available. Similar calculations can be carried out for annihilation to WW, ZZ, hh, which in fact dominate at large m_ϕ. In conclusion, as anticipated pNGB DM undergoes s-wave annihilation to SM particles.

DM-nucleon elastic scattering

To calculate the cross section for DM scattering on nucleons, one starts from the parton-level amplitude for $\phi q \to \phi q$,

$$\mathscr{M} = \sum_q \frac{i}{t-m_h^2}\left(\frac{c_d}{f^2}t\right)m_q\bar{u}_q(p_4)u_q(p_2)\,, \tag{2.9}$$

which immediately shows the very strong suppression of the direct detection rate: since $t \sim m_\phi^2 v_{\mathrm{DM}}^2$, the cross section ends up being proportional to $v_{\mathrm{DM}}^4 \sim 10^{-12}$ for scattering on Earth. We thus postpone a complete calculation of the DM-nucleon cross section to the discussion of the marginal Higgs portal in Section 2.2.

Higgs decay to a DM pair

If $m_\phi < m_h/2 \approx 62.5$ GeV, the derivative portal also leads to Higgs boson decay to an invisible DM pair. The squared amplitude for $h \to \phi\phi$ reads

$$\left|\overline{\mathscr{M}}\right|^2 = \left(\frac{c_d}{f^2} m_h^2\right)^2 v^2 \,, \tag{2.10}$$

leading to

$$\Gamma(h \to \phi\phi) = \frac{v^2}{32\pi m_h} \sqrt{1 - \frac{4m_\phi^2}{m_h^2}} \left(\frac{c_d}{f^2} m_h^2\right)^2 \,, \tag{2.11}$$

where one needs to recall that the final state involves identical particles.

Vector boson fusion at colliders

If $m_\phi > m_h/2$, DM pair production at colliders needs to proceed through an off-shell Higgs. The most promising process to test this is vector boson fusion (VBF), $VV \to h^* \to \phi\phi$. Since the Higgs boson only couples to the longitudinal polarizations of the vector bosons, the amplitude of the process is

$$\mathscr{M} = -\left(1 - \frac{m_h^2}{s}\right)^{-1} \frac{i c_d}{f^2} v^2 \epsilon^\mu_{V,\lambda}(p_1) \epsilon_{\mu V,\lambda'}(p_2) \frac{g^2}{2} \,. \tag{2.12}$$

The unpolarized squared matrix element reads

$$\left|\overline{\mathscr{M}}\right|^2 = \left(1 - \frac{m_h^2}{s}\right)^{-2} \frac{c_d^2}{f^4} v^4 \frac{g^4}{4} \left(-\eta^{\mu\nu} + \frac{p_1^\mu p_1^\nu}{M_V^2}\right) \left(-\eta_{\mu\nu} + \frac{p_{2\mu} p_{2\nu}}{M_V^2}\right) \simeq \left(1 - \frac{m_h^2}{s}\right)^{-2} \frac{c_d^2 s^2}{f^4} \,, \tag{2.13}$$

where the last line comes from the assumption of $s \gg M_V^2$.

Since we assume an high-energy fusion, we can approximate massless initial bosons: thus in the center of mass frame the differential cross section reads

$$\frac{\mathrm{d}\sigma}{\mathrm{d}\Omega} = \frac{1}{64\pi^2} \left(1 - \frac{4m_\phi^2}{s}\right)^{\frac{1}{2}} \frac{\left|\overline{\mathscr{M}}\right|^2}{s} \,. \tag{2.14}$$

Substituting and integrating over the phase space, one arrives at [40]

$$\sigma(VV \to \phi\phi) = \frac{1}{32\pi} \frac{c_d^2 s}{f^4} \left(1 - \frac{4m_\phi^2}{s}\right)^{\frac{1}{2}} \left(1 - \frac{m_h^2}{s}\right)^{-2} \,. \tag{2.15}$$

Notice the growth $\propto s$ of this cross section.

2.1.2 Phenomenological results

Constraint from DM relic density

The first constraint we impose on the model is that $\langle\sigma v\rangle$ yields the correct DM relic abundance today as measured by Planck, $\Omega_{\rm DM} h^2 = 0.1200 \pm 0.0012$ [6]. To do so all annihilation channels to fermions must be included using (2.8), as well as annihilations to WW, ZZ, hh. The full calculation goes beyond the scope of this thesis and we simply make use of the results presented in [41], from which we take the contour reproducing the relic abundance for the derivative portal shown in Fig. 2.1. For $m_\phi \gtrsim 130$ GeV, a very simple relation determining the coupling strength in terms of m_ϕ can be obtained [41]

$$\frac{f}{c_d^{1/2}} \approx 1300 \text{ GeV} \left(\frac{m_\phi}{130 \text{ GeV}}\right)^{\frac{1}{2}} \,. \tag{2.16}$$

This is shown as a dashed orange line in Fig. 2.1. Notice that Ref. [41] considered complex scalar DM while here we have a real field, hence the observed relic abundance is obtained for a value $(f/c_d^{1/2})_{\rm here} = 2^{1/4} (f/c_d^{1/2})_{\rm there}$.

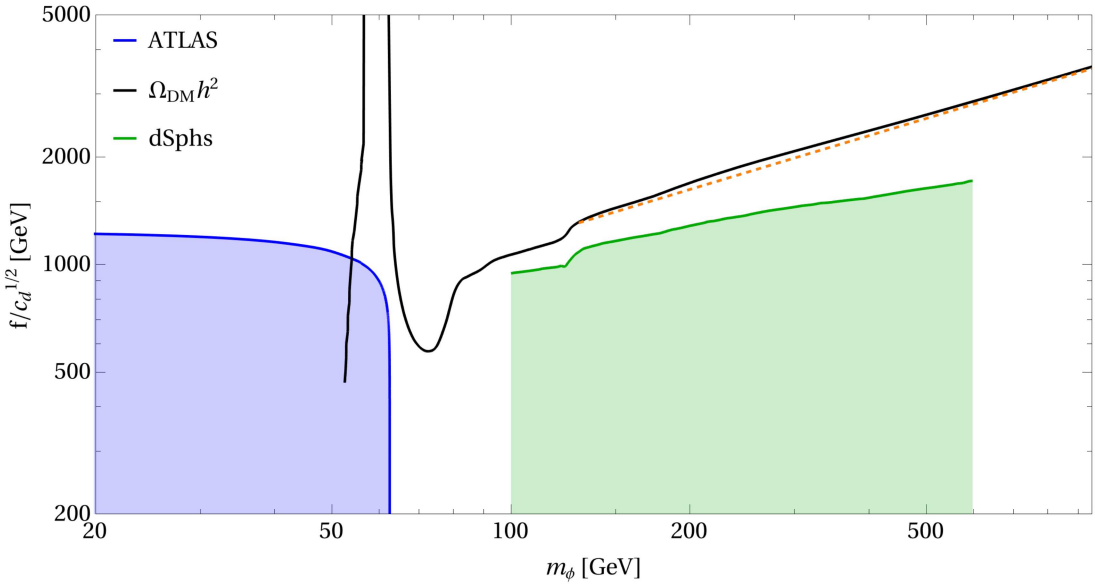

Figure 2.1: Parameter space for the derivative Higgs portal model, including current constraints from the DM relic abundance (black curve), Higgs invisible decays (blue region), and indirect detection in gamma rays (green region). The dashed orange line shows the approximate relation in Eq. (2.16).

(No) constraints from DM direct searches

As already stressed, the derivative portal predicts an extremely small direct detection rate, well below the neutrino floor. It will thus remain out of reach of direct searches for the foreseeable future.

Constraints from invisible Higgs decays

The Higgs boson was discovered in 2012 by the ATLAS and CMS collaborations, with the dominant sensitivity coming from the $h \to \gamma\gamma$ and $h \to ZZ^{(*)} \to 4\ell$ final states [42, 43]. Since then, progress has been made in testing many more Higgs decay channels. The one relevant here is the decay to invisible particles, for which the best current bound is BR(h $\to$ inv) < 0.11 at 95% CL by ATLAS [44].

To extract a bound on the pNGB parameter space we thus require

$$\mathrm{BR}(h \to \mathrm{inv}) = \frac{\Gamma\left(h \to \phi\phi\right)}{\Gamma^{\rm SM}_{\rm tot}(h) + \Gamma\left(h \to \phi\phi\right)} < 0.11\,, \tag{2.17}$$

where $\Gamma\left(h \to \phi\phi\right)$ was calculated in (2.11) and the total width predicted by the SM is $\Gamma^{\rm SM}_{\rm tot}(h) \approx 4.1$ MeV. The corresponding exclusion is shown in blue in Fig. 2.1.

Constraints from indirect detection experiments

Here again we simply adopt the bounds derived in [41] from the Fermi observations of dwarf galaxies [45], shown by the green region in Fig. 2.1.

Summary

Figure 2.1 presents the parameter space $\left(m_\phi, f/c_d^{1/2}\right)$. We see that the $h \to$ inv bound significantly constrains the region $m_\phi < m_h/2$, by requiring $f/c_d^{1/2} \gtrsim 1200$ GeV. Although not shown in the figure, indirect searches constrain a small region of masses $m_h/2 \lesssim m_\phi \lesssim 70$ GeV [41]. However, for masses $m_\phi \gtrsim 70$ GeV the thermal abundance line cannot be probed by existing experiments. As we are going to discuss in Chapter 5, a muon collider has the potential to change this situation.

2.2 Marginal Higgs portal

We now turn to the marginal Higgs portal of Eq. (2.2), for which the interplay between DM annihilation, scattering on nuclei, and production at colliders is markedly different.

2.2.1 Theoretical predictions

DM annihilation to SM particles

The amplitude for annihilation to SM fermions is given by (2.3) with $c_d s/f^2 \to -\lambda$, leading to

$$\langle \sigma_{\rm CM} v_{\rm rel} \rangle(T) \simeq \frac{m_f^2 \lambda^2}{64\pi\, m_\phi^4} \left(1 - \frac{m_f^2}{m_\phi^2}\right)^{3/2} \left(1 - \frac{m_h^2}{4m_\phi^2}\right)^{-2} . \tag{2.18}$$

Notice that annihilation to WW, ZZ, hh has a different scaling at large m_ϕ, namely $\langle \sigma_{\rm CM} v_{\rm rel} \rangle \sim \lambda^2/m_\phi^2$.

DM-nucleon elastic scattering

As we are interested in scattering at low momentum transfer we must go beyond the quark level, because the interaction effectively proceeds with the whole nucleon. We start with the perturbative amplitude for DM scattering on all the quarks in the nucleon,

$$\mathscr{M} = -\frac{i\lambda}{t - m_h^2} \sum_q m_q \bar{u}_q(p_4) u_q(p_2) \,, \tag{2.19}$$

which at hadronic level is modified to

$$\mathscr{M} = -\frac{i\lambda}{t - m_h^2} \langle N | \sum_{q\,=\,u,d,s} m_q \bar{u}_q u_q + \sum_{q\,=\,c,b,t} m_q \bar{u}_q u_q \, |N\rangle \, \overline{N}_{s'}(P') N_s(P) \,. \tag{2.20}$$

From the QCD Lagrangian, the following expression for the generic baryon mass is obtained [46–49]

$$m_N = \langle N | \, \Theta^\mu_\mu \, |N\rangle = \langle N | \sum_{q\,=\,u,d,s} m_q \bar{u}_q u_q + \sum_{q\,=\,c,b,t} m_q \bar{u}_q u_q + \frac{\beta}{4\alpha_s} G^a_{\mu\nu} G_a^{\mu\nu} \, |N\rangle \ , \tag{2.21}$$

where $\beta = -\frac{7\alpha_s^2}{2\pi}$. Since the heavy quarks contribute via one-loop triangle diagrams with external gluons, we replace

$$\sum_{q\,=\,c,b,t} m_q \bar{u}_q u_q \simeq -\frac{\alpha_s}{4\pi} G^a_{\mu\nu} G_a^{\mu\nu} \,, \tag{2.22}$$

In particular, combining the hadronic matrix element (2.20) with (2.21) and (2.22) we find

$$\langle N | \sum_{q\,=\,u,d,s} m_q \bar{u}_q u_q + \sum_{q\,=\,c,b,t} m_q \bar{u}_q u_q \, |N\rangle \simeq \frac{2}{9} m_N + \frac{7}{9} \langle N | \sum_{q\,=\,u,d,s} m_q \bar{u}_q u_q \, |N\rangle \ . \tag{2.23}$$

The last term can then be written as

$$\langle N | \sum_{q\,=\,u,d,s} m_q \bar{u}_q u_q \, |N\rangle = \sum_{q\,=\,u,d,s} \sigma_q = m_N \sum_{q\,=\,u,d,s} f^N_{T_q} \,, \tag{2.24}$$

where $\sigma_q \equiv \langle N | \, m_q \bar{u}_q u_q \, |N\rangle$ is the quark sigma term of the nucleon, usually expressed in DM studies in terms of the form factors $f^N_{T_q} \equiv \frac{\sigma_q}{m_N}$. Applying these results and averaging over proton and neutron contributions, the DM-nucleon elastic scattering amplitude becomes

$$\mathscr{M} = -\frac{i\lambda}{t - m_h^2} \frac{1}{A} \left[Z m_p f_p + (A - Z) m_n f_n \right] \overline{N}_{s'}(P') N_s(P) \,, \tag{2.25}$$

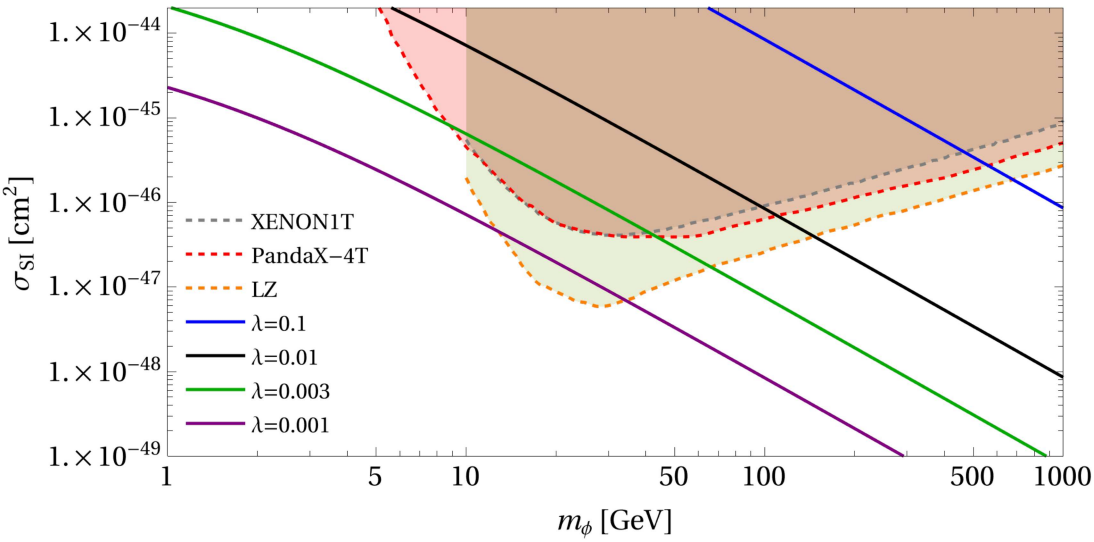

Figure 2.2: Comparison of the theoretical prediction of the spin-independent DM-nucleon scattering cross sections as derived from the marginal Higgs portal (colored curves), with the regions excluded at 90% CL by the three most recent Xenon-based direct detection experiments (shaded regions).

where $f_N \equiv \frac{2}{9} + \frac{7}{9}\sum_{q=u,d,s} f_{T_q}^N$. For $^{131}_{54}$Xe, one has $A = 131$ and $Z = 54$. Squaring the matrix element gives

$$\left|\overline{\mathscr{M}}\right|^2 \simeq \frac{4m_N^2\lambda^2}{m_h^4 A^2}\left[Zm_p f_p + (A-Z)m_n f_n\right]^2 , \tag{2.26}$$

where we have neglected the small momentum exchange t. For elastic scattering we have in the center of mass frame

$$\frac{\mathrm{d}\sigma_{\mathrm{CM}}}{\mathrm{d}\Omega} = \frac{1}{64\pi^2}\frac{\left|\overline{\mathscr{M}}\right|^2}{s} , \tag{2.27}$$

and since $s = (p_1 + P)^2 \simeq (m_\phi + m_N)^2$ in the nonrelativistic limit, we arrive at the final result

$$\sigma_{\phi N} = \frac{1}{4\pi}\left(\frac{m_\phi m_N}{m_\phi + m_N}\right)^2 \frac{\lambda^2}{m_\phi^2 m_h^4 A^2}\left[Zm_p f_p + (A-Z)m_n f_n\right]^2 \simeq \frac{1}{4\pi}\left(\frac{m_\phi m_N}{m_\phi + m_N}\right)^2 \frac{\lambda^2 m_N^2 \bar{f}_N^2}{m_\phi^2 m_h^4} , \tag{2.28}$$

where in the last step we have made the approximations $m_p \approx m_n \approx m_N$ and $f_p \approx f_n \approx \bar{f}_N \approx 0.30$. Differently from the derivative portal, for the marginal portal the direct detection rate is not suppressed by the momentum transfer. As we are going to show, this implies strong constraints on λ.

Higgs decays to a DM pair and vector boson fusion at colliders

In complete analogy with (2.11) we obtain a decay width

$$\Gamma(h \to \phi\phi) = \frac{v^2\lambda^2}{32\pi m_h}\sqrt{1 - \frac{4m_\phi^2}{m_h^2}} . \tag{2.29}$$

Similarly, for VBF production of DM with $m_\phi > m_h/2$ we find

$$\sigma(VV \to \phi\phi) = \frac{\lambda^2}{32\pi s}\left(1 - \frac{4m_\phi^2}{s}\right)^{\frac{1}{2}}\left(1 - \frac{m_h^2}{s}\right)^{-2} . \tag{2.30}$$

In contrast with Eq. (2.15), this cross section is proportional to $1/s$ and therefore suppressed at large energies.

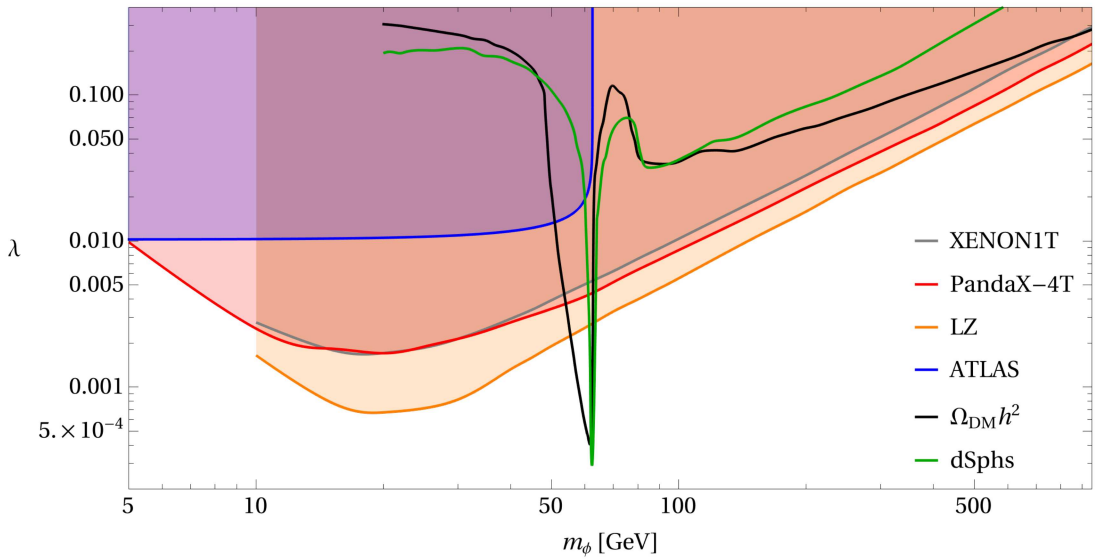

Figure 2.3: Parameter space for the marginal (also known as renormalizable) Higgs portal model, including current constraints from the DM relic abundance (black curve), Higgs invisible decays (blue region), indirect detection in gamma rays (green curve; the excluded region lies above it) and direct detection experiments (remaining colored regions).

2.2.2 Phenomenological results

Constraints from DM relic density and indirect detection experiments

For the thermal relic density curve and the indirect detection constraints, we use directly the results of the recent study [50]. They are shown by the black and green curves in Fig. 2.3, respectively.

Constraints from DM direct searches

Direct DM searches represent the strongest source of constraints on the marginal Higgs portal. We consider here the results coming from three already-mentioned experiments, namely XENON1T [27], PandaX-4T [28], and LZ [29], which has reached the best sensitivity to date. Further improvements are expected in the near future. From Eq. (2.28) we obtain a theoretical prediction for DM scattering via the marginal Higgs portal

$$\sigma_{\phi N} \simeq 8.7 \times 10^{-43}\ \text{cm}^2\, \lambda^2 \left(\frac{m_\phi}{100\ \text{GeV}}\right)^{-2}\,, \tag{2.31}$$

valid in the regime $m_\phi \gg m_N \sim$ GeV.

In Fig. 2.2 the predicted cross sections are compared to the experimental bound, as a function of m_ϕ for a few benchmark values of λ in the range between 0.001 and 0.1. We stress that these values of the portal coupling do not, in general, yield the correct thermal abundance from freezeout. Nevertheless, this comparison is very interesting, as one may realize scenarios where the freezeout is dominantly mediated by the derivative portal, while a small λ generated by small explicit breakings of the DM shift symmetry mediates scattering on nuclei [51–53]. While $\lambda = 0.1$ is excluded for $m_\phi \lesssim 700$ GeV, smaller values $\lambda \sim O\big(10^{-3}\big)$ are still consistent with DM lighter than 100 GeV. In Fig. 2.3, the exclusions from direct detection are instead shown in the (m_ϕ, λ) plane.

Constraints from invisible Higgs decay

To obtain the parameter region excluded by Higgs invisible decay searches, we plug Eq. (2.29) into (2.17), obtaining the region shaded in blue in Fig. 2.3.

Summary

Figure 2.3 shows the (m_ϕ, λ) parameter space. At low masses, the $h \to$ invisible bound requires $\lambda \lesssim 0.010$. Indirect detection searches exclude the region above the green curve, and are currently important only for $m_\phi \lesssim 90$ GeV. Clearly, the most important role is played by direct detection searches, which exclude the thermal relic curve up to the largest value of m_ϕ shown in the figure. In fact, one can check that the latest LZ results rule out Higgs portal DM for $m_\phi < 2.8$ TeV (with the exception of a small region around the Higgs resonance, $m_\phi \sim m_h/2$), a severe exclusion that can be viewed as a further motivation to look at alternative thermal scenarios such as, minimally, the derivative Higgs portal.

Chapter 3

Composite Higgs models of pNGB dark matter

In this chapter we present, in an introductory manner, one of the main motivations for pNGB DM: models of composite dynamics at the TeV scale, where both the Higgs and DM fields arise together as pseudo-Goldstone bosons [51]. After some initial remarks, in Sec. 3.1 we show explicitly how, for the very popular class of global symmetry breaking patterns $SO(N)/SO(N-1)$, the kinetic term of the nonlinear sigma field automatically gives rise to the derivative Higgs portal interaction if $N > 5$. For an extensive discussion of the composite Higgs framework, and many important references, see [54].

Composite Higgs theories are one of the main proposed solutions to the electroweak hierarchy problem (the other major class being supersymmetric theories), namely the question why $m_h \sim 100$ GeV is so much smaller than other physical scales in Nature, such as for instance the Planck scale $M_{\rm Pl}$. Composite Higgs models solve this difficulty by means of dimensional transmutation, which can dynamically generate hierarchies of scales. The strong scale of the new interaction, called here Λ, cannot be lighter than several TeV due to experimental constraints from low-energy precision measurements and LHC searches. Therefore, to accommodate a Higgs as light as the observed one a further assumption is made, namely that the Higgs field H is described as a set of four (pseudo-)Goldstone bosons arising from a spontaneous global symmetry breaking in the new strongly interacting sector. This naturally sets $m_h \ll \Lambda$.

To obtain a custodially invariant SM at low energies, the minimal symmetry breaking pattern is $SO(5)/SO(4)$, which has been studied in great detail, see [55–68] for a partial list of references. However, from a bottom-up perspective non-minimal cosets appear equally motivated. Then, the additional Goldstone bosons that accompany the Higgs may serve as thermal DM candidates, provided they are stabilized by some (discrete or continuous) symmetry. Such extended composite Higgs models can solve the hierarchy and DM problems in one stroke, making them very appealing from a theoretical standpoint. We now briefly introduce the global symmetry structure and its spontaneous breaking in composite Higgs theories [54, 69].

Symmetry breaking structure

In general, we suppose the new composite sector to be characterized by a global symmetry group $\mathscr{G}$, which is spontaneously broken at scale f as $\mathscr{G} \to \mathscr{H}_1$. We can think of f as analogous to the pion decay constant in low-energy QCD. The spontaneous symmetry breaking gives rise to a set of Goldstone bosons. To describe the interactions of the transverse SM gauge bosons, a subgroup $\mathscr{H}_0 \subset \mathscr{G}$ is weakly gauged. In the simplest case, one can identify $\mathscr{H}_0$ with the electroweak group of the SM, $SU(2)_L \times U(1)_Y$. As a consequence, $\mathscr{H} = \mathscr{H}_1 \cap \mathscr{H}_0$ is the final unbroken gauge group, and we find $n = \dim(\mathscr{G}) - \dim(\mathscr{H}_1)$ Goldstone bosons, of which $n_0 = \dim(\mathscr{H}_0) - \dim(\mathscr{H})$ are eaten to become longitudinal polarizations of massive vector bosons, whereas $n - n_0$ remain in the spectrum as physical pNGBs. Conditions for a viable model are that the electroweak gauge group can be embedded into

the unbroken $\mathscr{H}_1$, and that the coset $\mathscr{G}/\mathscr{H}_1$ contains at least one $SU(2)_L$ doublet which is identified with H.

The global symmetry is explicitly broken at least by the weak SM gauging and by the fermionic operators which are at the origin of the SM Yukawas. As a result the Higgs field h acquires a radiative potential, which in turn triggers electroweak symmetry breaking,

$$v = f \sin \frac{\langle h \rangle}{f} \,, \tag{3.1}$$

realizing vacuum misalignment. For $v \ll f$, the properties of the Higgs approach those it possesses in the SM. While a large hierarchy requires a high degree of fine-tuning and thus goes against the spirit of the construction, in practice $f/v \sim 3\text{-}4$ yields a realistic theory, where the Higgs couplings deviate from the SM at $O(v^2/f^2)$. Such moderate hierarchy between f and v is usually obtained at the price of a "residual" cancellation in the Higgs potential.

3.1 An example: $SO(N)/SO(N-1)$ coset

As we already mentioned, the minimal coset accommodating the custodial SM is $SO(5)/SO(4)$. The extension of this coset to $SO(N)/SO(N-1)$, which gives rise to $N-1$ Goldstone bosons, plays an important role in building models of pNGB DM. The minimal step is to consider $SO(6)/SO(5)$, where the Higgs doublet is accompanied by a real SM singlet scalar. A discrete $\mathbb{Z}_2$ symmetry can stabilize the singlet, rendering it a DM candidate.

To see how the derivative Higgs portal automatically arises in $SO(6)/SO(5)$, we parametrize the Goldstone bosons π_a $(a = 1, \ldots, 5)$ by means of the field

$$\phi = \exp\left[i \frac{\pi_a \hat{T}^a}{f} \sqrt{2} \right] \phi_0 \,, \tag{3.2}$$

where $\hat{T}^a_{ij} = -\frac{i}{\sqrt{2}}(\delta^a_i \delta^6_j - \delta^a_j \delta^6_i)$ and

$$\phi_0 = \begin{pmatrix} 0 & 0 & 0 & 0 & 0 & 1 \end{pmatrix}^T \,. \tag{3.3}$$

Notice that ϕ transforms in the fundamental representation of $SO(6)$. Defining $\vec{\pi} = (h_i, \eta)$, where η represents the pNGB DM candidate, we have

$$i \frac{\pi_a \hat{T}^a}{f} \sqrt{2} = \frac{1}{f} \begin{pmatrix} 0 & 0 & 0 & 0 & 0 & h_1 \\ 0 & 0 & 0 & 0 & 0 & h_2 \\ 0 & 0 & 0 & 0 & 0 & h_3 \\ 0 & 0 & 0 & 0 & 0 & h_4 \\ 0 & 0 & 0 & 0 & 0 & \eta \\ -h_1 & -h_2 & -h_3 & -h_4 & -\eta & 0 \end{pmatrix} \,. \tag{3.4}$$

By explicit calculation, the following form is obtained

$$\phi = \sin \frac{|\vec{\pi}|}{f} \begin{pmatrix} \frac{h_1}{|\vec{\pi}|} & \frac{h_2}{|\vec{\pi}|} & \frac{h_3}{|\vec{\pi}|} & \frac{h_4}{|\vec{\pi}|} & \frac{\eta}{|\vec{\pi}|} & \cot \frac{|\vec{\pi}|}{f} \end{pmatrix}^T \tag{3.5}$$

and applying the field redefinition $\sin \frac{|\vec{\pi}|}{f} \frac{\pi_a}{|\vec{\pi}|} \to \frac{\pi_a}{f}$, we finally arrive at

$$\phi = \begin{pmatrix} \frac{h_1}{f} & \frac{h_2}{f} & \frac{h_3}{f} & \frac{h_4}{f} & \frac{\eta}{f} & \sqrt{1 - \frac{|h|^2 + \eta^2}{f^2}} \end{pmatrix}^T \,. \tag{3.6}$$

The leading, two-derivative term of the Goldstone Lagrangian reads

$$\begin{aligned} \partial_\mu \phi^T \partial^\mu \phi &= \frac{1}{f^2} \sum_{i=1}^{4} \partial_\mu h_i \partial^\mu h_i + \frac{1}{f^2} \partial_\mu \eta \partial^\mu \eta + \frac{1}{4f^4} \left(1 - \frac{|h|^2 + \eta^2}{f^2} \right)^{-1} \left(\partial_\mu |h|^2 + \partial_\mu \eta^2 \right)^2 \\ &\simeq \frac{2}{f^2} \partial_\mu H^\dagger \partial^\mu H + \frac{1}{f^2} \partial_\mu \eta \partial^\mu \eta + \frac{1}{f^4} \partial_\mu |H|^2 \partial^\mu |H|^2 + \frac{1}{4f^4} \partial_\mu \eta^2 \partial^\mu \eta^2 + \frac{1}{f^4} \partial_\mu |H|^2 \partial^\mu \eta^2 \,, \end{aligned} \tag{3.7}$$

where in the second line we have retained terms up to second order in the $1/f^2$ expansion. Hence,

$$\mathscr{L}_2 = \frac{f^2}{2}\partial_\mu\phi^T\partial^\mu\phi \simeq \partial_\mu H^\dagger\partial^\mu H + \frac{1}{2}\partial_\mu\eta\partial^\mu\eta + \frac{1}{2f^2}\partial_\mu|H|^2\partial^\mu|H|^2 + \frac{1}{8f^2}\partial_\mu\eta^2\partial^\mu\eta^2 + \frac{1}{2f^2}\partial_\mu|H|^2\partial^\mu\eta^2\,. \tag{3.8}$$

As advertised, we have thus obtained the derivative portal operator that couples H and η.

3.2 Brief review of models

$SO(6)/SO(5)$ coset

The first introduction of the model can be found in [70] where the authors considered the advantages of this non-minimal composite Higgs model. Without performing an explicit reference to WIMP candidate, it is explained that the presence of an electroweak singlet η NGB along the composite Higgs significantly modifies the phenomenology, in terms of their annihilation through $h^2\eta^2$ coupling that influences the relic density computation. [68] proposes a way to embed the fermionic fields in the described coset, highlighting the possibility to get a stable DM candidate. An important consequence is the focus on the SM coupling modifications in terms of the tuning parameter $\xi = v^2/f^2$. The first in-depth focus on pNGB DM within the $SO(6)/SO(5)$ coset comes in [51], where derivative and marginal portals are tested using data from relic density, Higgs searches at LHC and DM searches. A relevant study on the loop-induced Higgs potential is included in [71], where contributions from gauge bosons and top quark loops are presented, along with effects from $SU(4)$ explicit breaking (recall that $SU(4)/Sp(4) \cong SO(6)/SO(5)$). A similar analysis is included in [72]. Furthermore we can also check the presence of phenomenological aspects related to LHC and astrophysics. The former takes into account the invisible Higgs decays with modified couplings, but more interestingly they analyzed the presence of expected composite resonances that would arise. On the other hand, typical astrophysics constraints are found in the relic density, direct and indirect detection experiments. Similar content is found in [73], where three distinguished sources of indirect detection constraints are analyzed. The section dedicated to collider phenomenology presents inputs from Higgs measurements, from heavy scalar searches and from the effects on EW precision tests. In [74] the DM shift symmetry is broken only softly by the top sector, in order to suppress the marginal portal coupling and be consistent with direct detection requirements. The parameter space of the theory is analyzed by means of relic density, Fermi-LAT and XENON1T data. In particular the major interest is reserved for the spin-independent cross section for the elastic scattering between DM and nucleons, which escapes the constraints from experimental bounds.

$SO(7)/SO(6)$ coset

The references [53, 75–78] discuss the model of composite pNGB Higgs and DM based on $SO(7)$ spontaneously broken down to $SO(6)$. This leads to 6 Goldstone bosons, thus 2 real scalars in addition to the Higgs doublet. Reference [75] chooses embeddings for the SM fermions such that the singlet η is stable and therefore a DM candidate, while the second singlet κ receives a negative mass term, leading it to develop a vev and favor a strong electroweak phase transition. As far as phenomenology is concerned, two parameter regimes are analyzed and it is pointed out that the dominant DM annihilation process would be $\eta\eta \to \kappa\kappa$. Reference [53] considered a complex scalar DM candidate: the fermion embedding and the potential construction are followed by a section on phenomenology, with bounds from relic abundance, direct and indirect detection. Finally the collider section studies the effects of top partners on Higgs coupling modifications. The same authors published a further paper [41] where two scenarios are presented: the first one where the global symmetry is explicitly broken by light quark interactions, and the second one where the breaking is caused by the gauging of the stabilizing $U(1)$ symmetry. These have different phenomenological implications, in particular with possible probes coming from collider, cosmology and astroparticle experiments. In [76] the interest is on the low energy effects of the model presented, then the phenomenology of new expected states is studied, while still considering the effects on Higgs physics. The subsequent [78] contains a study

of collider signals that are expected from the model. The two pNGBs singlets are called η (the DM candidate) and κ (extra singlet). They focused on processes such as $\kappa\kappa \to \gamma\gamma b\bar{b}$, $\kappa\kappa \to b\bar{b}b\bar{b}$, and $\kappa\kappa \to \mu^+\mu^-\mu^+\mu^-$, which test both the compositeness and the non-minimality of the model. These probes would be relevant in the cases where DM escapes the ordinary searches, even at future colliders. Finally we note reference [77], where the coset is included into a neutral naturalness framework: this results in the addition of new fields, which seriously affect the phenomenology, in particular at the LHC.

Composite pNGB 2 Higgs doublet models

Up to now we only considered models where a single Higgs doublet was present, but it is possible that a pair of them originate from the breaking of a larger global symmetry group, giving rise to a composite two-Higgs doublet model (2HDM). A first example is given in [79] where the coset is $SU(4)\times SU(4)/SU(4)$. We can check how the presence of an additional Higgs field modifies the mechanism of electroweak symmetry breaking. We mention that the authors included a study on the massive composite resonances that would emerge, whose presence might be tested at future colliders. A related model was investigated in an earlier work [80]. In [81] a different coset is proposed, $SU(6)/SO(6)$, and here we find phenomenological implications that involve the EW precision test parameters S and T. Besides this, it also considers the presence of many more new light singlets. The final example in [82] studies the $SO(7)/SO(5)\times SO(2)$ breaking, and beyond precision tests it also includes results from direct and indirect detection, invisible Higgs decay and the relic density, where the latter is also affected by the presence of an extra pNGB.

$SO(7)/G_2$ coset

The paper [83] adopts a fermion embedding in a group representation such that the effective potential is generated by fermionic loops, dominated by the top contribution. Deviations in $h \to \gamma\gamma$ are analyzed by varying the mass and couplings of the light charged scalar that arises in the spectrum. This new resonance is relevant for LHC phenomenology, decaying into $t\bar{b}$ if heavy enough. Reference [84] brings a second example where the same coset is adopted. It is here highlighted that such framework can provide two different types of DM candidates: it can be a scalar real triplet or singlet, depending on the way in which the weak gauging procedure is performed. The triplet scenario is studied in most of the paper, while for the singlet they provide a final section where differences are pointed out. They calculate the Higgs production and decay into photons, comparing them to LHC measurements to obtain bounds on f. Further phenomenological aspects concern direct and indirect searches and the thermal cross section for DM annihilation, in order to constrain the model from the relic abundance. Finally, for the singlet case, exploiting LHC does not seem very promising, while the reach is expected to improve at future colliders.

Other models

Reference [85] does not perform an explicit study of pNGB DM, but rather covers models where 2 composite Higgs doublets arise as NGBs, which may in general contain a DM candidate. The phenomenological aspect considered is the modification of the T parameter in different cosets leading to 2HDMs. The electroweak precision parameter results to be affected already at tree level. The paper [86] tries to embed a composite pNGB Higgs and DM model within a Grand Unified Theory (GUT) symmetry group, selecting $SU(7)/SU(6)\times U(1)$. The parameter space is constrained only from direct detection, while other regions are excluded by means of theoretical arguments. On the other hand, an extended section is dedicated to the large amount of exotic states that characterize the model. A second proposal involving the embedding of a composite Higgs into a GUT appeared in [87], where the framework is represented by a supersymmetric 6D theory, based on the gauge group $E_6 \times G_0$. Effects could be found in the T parameter and also in the top quark couplings, but these seem to be too small to be tested. On the other hand, signatures could be obtained from hypothetical exotic states at the TeV scale. In [88], the patterns $SU(3)/SU(2)\times U(1)$ and $SU(2)\times SU(2)\times U(1)/SU(2)\times U(1)$ are considered. The relic density constraints are able to provide

by themselves the most important contribution, since the limits from EW precision tests turn out to be weak. Also collider studies on long-lived particles and heavy resonances are significant, due to their complementarity with the non-collider bounds. The pattern $SU(4) \times SU(4)/SU(4)$ is used in [80], with the hypothesis of composite pNGB DM and Higgs. The phenomenology of the scalar sector with 11 exotic pNGBs is explored, by means of mono-X searches and DM production channels at LHC. An interesting phenomenological analysis is found in [89], where we see the features of a littlest Higgs model with $T-$parity and $SU(5)/SO(5)$ coset. Firstly, the combination of bounds from EW precision tests and LHC phenomenology on top partner masses gives an initial hint on the forbidden parameter space. The analysis of the pNGB DM singlet is developed by confronting the main experimental data, and comparing the cases where the candidate is elementary or composite. Finally, we report the example of [90] where generic models invariant under a $SU(4) \times SU(2) \times U(1)$ symmetry are considered. Three scenarios appear, distinguished by the way in which the SM fermion masses are generated, with significant impact on the phenomenology.

Chapter 4

Elementary Higgs models of pNGB dark matter

We discuss here a second class of models that gives rise to pNGB DM, which at low energies couples to the SM via the derivative Higgs portal. These are scalar extensions of the SM, characterized by global symmetries, which are explicitly broken only by suitably-chosen operators. Importantly, in these models only the DM is a pNGB, while the Higgs is not, which implies that the electroweak hierarchy problem is not addressed.

To make the exposition concrete, let us consider the simplest case [91–93]: we extend the SM by a single complex scalar field S,

$$\mathscr{L} = \mathscr{L}_{\rm SM} + \mathscr{L}_S \,, \tag{4.1}$$

where

$$\mathscr{L}_S = |\partial_\mu S|^2 + \frac{\mu_S^2}{2}|S|^2 - \frac{\lambda_S}{2}|S|^4 - \lambda_{HS}|S|^2|H|^2 + \frac{\mu_S'^2}{4}\left(S^2 + S^{*2}\right) \,, \tag{4.2}$$

where we recognize a potential for S that spontaneously breaks the $U(1)$ symmetry ($\mu_S^2, \lambda_S > 0$), a renormalizabile Higgs portal interaction, and an explicit $U(1)$ breaking piece. Introducing the radial and angular modes, $S = (v_s + \sigma)\exp(i\phi/v_s)/\sqrt{2}$ where v_s is the vev that leads to SSB, we identify ϕ with the pNGB, whose mass will come from $\mu_S'^2$ as we are going to discuss. We can rewrite Eq. (4.2) as

$$\begin{aligned}\mathscr{L}_S =& \frac{1}{2}\partial_\mu\sigma\partial^\mu\sigma + \frac{1}{2}\partial_\mu\phi\partial^\mu\phi\left(1+\frac{\sigma}{v_s}\right)^2 + \frac{\mu_S^2}{2}\frac{(v_s+\sigma)^2}{2} - \frac{\lambda_S}{2}\frac{(v_s+\sigma)^4}{4} + \\ &- \lambda_{HS}\frac{(v_s+\sigma)^2}{2}|H|^2 + \frac{\mu_S'^2}{4}(v_s+\sigma)^2\cos\left(\frac{2\phi}{v_s}\right) \,.\end{aligned} \tag{4.3}$$

Expanding this up to the quadratic order in σ and neglecting constant terms, we obtain

$$\begin{aligned}\mathscr{L}_S =& \frac{1}{2}\partial_\mu\sigma\partial^\mu\sigma + \frac{1}{2}\partial_\mu\phi\partial^\mu\phi\left(1+\frac{\sigma}{v_s}\right)^2 - \frac{1}{2}m_\sigma^2\sigma^2 + \\ &- \lambda_{HS}\frac{(v_s+\sigma)^2}{2}|H|^2 + \frac{\mu_S'^2}{4}(v_s+\sigma)^2\cos\left(\frac{2\phi}{v_s}\right) + O\left(\sigma^3\right) \,,\end{aligned} \tag{4.4}$$

where we defined

$$m_\sigma^2 = \frac{3}{2}\lambda_S v_s^2 - \frac{\mu_S^2}{2} \simeq \lambda_S v_s^2 \,, \tag{4.5}$$

where the last equality holds as a result of the vacuum condition for the leading S potential, $\mu_S^2 - \lambda_S v_s^2 \simeq 0$. Now, suppose that the radial mode σ is heavy enough that it can be integrated out. To do so, we derive from Eq. (4.4) its classical equation of motion

$$\sigma = \left[m_\sigma^2 + \Box - \frac{\Delta}{v_s}\right]^{-1} \cdot \Delta \,, \tag{4.6}$$

where

$$\Delta \equiv \frac{\partial_\mu \phi \partial^\mu \phi}{v_s} - \lambda_{HS} v_s \left|H\right|^2 + \frac{\mu_S'^2}{2} v_s \cos\left(\frac{2\phi}{v_s}\right) . \tag{4.7}$$

The effective Lagrangian is obtained by replacing the solution (4.6) into the Lagrangian (4.4),

$$\begin{aligned}
\mathscr{L}_{\rm EFT} =& \frac{1}{2}\partial_\mu\phi\partial^\mu\phi - \lambda_{HS}\frac{v_s^2}{2}|H|^2 + \frac{\mu_S'^2}{4}v_s^2\cos\left(\frac{2\phi}{v_s}\right) + \frac{1}{2}\Delta\frac{1}{\left[m_\sigma^2 + \Box - \frac{\Delta}{v_s}\right]}\Delta \\
\simeq& \frac{1}{2}\partial_\mu\phi\partial^\mu\phi - \frac{\mu_S'^2}{2}\phi^2 + \frac{1}{2}\Delta\frac{1}{m_\sigma^2}\Delta - \frac{1}{2m_\sigma^4}\lambda_{HS}^2 v_s^2 \left|H\right|^2 \Box \left|H\right|^2 \\
\simeq& \frac{1}{2}\partial_\mu\phi\partial^\mu\phi - \frac{\mu_S'^2}{2}\phi^2 + \frac{1}{2m_\sigma^2}\left[-2\partial_\mu\phi\partial^\mu\phi\lambda_{HS}\left|H\right|^2 + 2\lambda_{HS}\mu_S'^2\phi^2\left|H\right|^2\right] + \frac{1}{2m_\sigma^2}\frac{\lambda_{HS}^2}{\lambda_S}\partial_\mu\left|H\right|^2\partial^\mu\left|H\right|^2 .
\end{aligned} \tag{4.8}$$

where pieces that correct the SM Lagrangian were dropped, and higher order terms neglected. notice that the squared mass of ϕ is equal to $\mu_S'^2$, as we had anticipated. Finally we redefine the pNGB as

$$\phi \to \phi\left(1 + \frac{\lambda_{HS}\left|H\right|^2}{m_\sigma^2}\right) , \tag{4.9}$$

and thereby obtain

$$\mathscr{L}_{\rm EFT} \simeq \frac{1}{2}\partial_\mu\phi\partial^\mu\phi - \frac{\mu_S'^2}{2}\phi^2 + \frac{\lambda_{HS}}{2m_\sigma^2}\partial_\mu\phi^2\partial^\mu\left|H\right|^2 + \frac{\lambda_{HS}^2}{2m_\sigma^2\lambda_S}\partial_\mu\left|H\right|^2\partial^\mu\left|H\right|^2 . \tag{4.10}$$

This demonstrates that, at low energies, ϕ indeed couples to the Higgs via the familiar derivative portal operator.

Some useful considerations can be offered by comparing the size of the derivative portal to the one of the $\partial^2|H|^4$ operator, which we see is also generated in Eq. (4.10), and controls Higgs coupling deviations by renormalizing the Higgs wavefunction. In fact, by comparison with Eq. (2.1) we identify $1/f^2 = \lambda_{HS}/m_\sigma^2$. Then, the coefficient of the $\partial^2|H|^4$ operator reads

$$\frac{\lambda_{HS}}{\lambda_S}\frac{1}{f^2} , \tag{4.11}$$

suggesting that two different regimes exist:

- if $\lambda_{HS} \simeq \lambda_S$, the two operators are basically suppressed by the same scale. This regime reproduces the composite Higgs scenario, where Higgs coupling measurements provide an important complementary path to probe the theory;
- if $\lambda_{HS} \ll \lambda_S$, then the Higgs coupling corrections are parametrically suppressed compared to the derivative portal. As a consequence, direct probes of the derivative portal are relatively more important. This regime is specific to the scenario we consider in this section, where H is an elementary field.

To conclude, we point out that in this model the suppression of DM-nucleon scattering amplitude by t applies even if the radial mode is light and cannot be integrated out. The assumed specific form of the explicit breaking, namely $S^2 + S^{*\,2}$, is essential to obtain this suppression. Having illustrated the main idea behind this class of pNGB DM models, we turn to a short review of the existing literature on the subject.

4.1 Brief review of models

Global $U(1)$

The first paper to discuss the minimal model presented above was [91]. A complex scalar singlet is added to the SM and the most general potential is reported; however, odd powers of the new

field can be removed by imposing a discrete $\mathbb{Z}_2$ symmetry. From the resulting potential, four different possibilities are studied depending on the presence of a non-vanishing vev for the singlet and the way in which the $U(1)$ is or is not broken explicitly. Reference [92] considered constraints from many sources, including EW precision tests and the DM relic density, but mainly focused on direct detection: three mass ranges were taken into account and confronted with experimental data from the XENON100, CoGENT and DAMA/LIBRA collaborations. In [94] a theoretical analysis based on renormalization group evolution is implemented, deriving with bounds from EW precision tests, the analysis of the electroweak phase transition, direct detection data, the relic abundance, and colliders. Finally we note [95], which completely focuses on the possibility of probing the model at the LHC.

Several references discussed the potential of the model to realize electroweak baryogenesis together with DM, including [96, 97]. Reference [98] discussed the possibility to also embed inflationary dynamics. When a first order electroweak phase transition is required, the presence of a stochastic gravitational wave (GW) background is expected, thus yielding another testable prediction. A second work that places its focus on GW signals is [99]. In [100] it is shown that the cancellation in direct detection can only be obtained in regions of parameters with a second order phase transition. Vice versa, [101] does not completely rule out a first order transition, although confirming that this would imply couplings that enhance the direct detection cross section. The paper [102] considers the effects of early kinetic decoupling, focusing its attention on the Higgs resonance region. The effect of the decoupling appears to be significant not only for the interaction strength, but also for invisible Higgs decays. Another phenomenological paper [103] is focused on the tentative excesses in the spectra of cosmic gamma rays and antiprotons, respectively from the Fermi-LAT and AMS collaborations. A possible explanation is found in pNGB DM annihilation to $b\bar{b}$, respecting simultaneously the other constraints such as the cancellation in DM-nucleon elastic scattering.

Loop level diagrams mediating direct detection processes, and their effect on the spin independent cross section, have been considered in several studies. In [104] the global $U(1)$ is broken down to residual $\mathbb{Z}_2$ and CP discrete symmetries. One loop EW correction to DM-nucleon scattering are calculated and compared with the expected reach of LZ. Similar studies were done in [105, 106]. Reference [107] studies the stability of the model under renormalization, up to two loops, and then discusses the effects on constraints at the electroweak scale. The more recent [108] is dedicated to direct detection phenomenology, showing how the cancellation appears when the two scalar mediators of the process are degenerate in mass: this scenario is then discussed in collider experiments, such as the proposed ILC at $\sqrt{s} = 250$ GeV. We finally mention [109], comparing XENON1T, PandaX-4T and LUX bounds on the model. Non-linear and linear parametrizations of the complex singlet are considered.

Gauged $U(1)$

In this type of models, the $U(1)$ is promoted to a local symmetry. In [110] the SM gauge group is extended by $U(1)_{B-L}$, and a scalar singlet with positive $B - L$ charge is added. The cancellation in direct detection is guaranteed, and they focused on stability of the DM candidate, since in this setup the pNGB is unstable. Two- and three-body decay widths are computed and compared with limits coming from perturbative unitarity and cosmic rays: finally the scalar is confirmed to be long-lived enough to be a viable candidate. An alternative solution is presented by [111], where a new SM singlet transforms under a global $SU(2)_g$ and a local $U(1)_X$. Calling V the new vector boson and χ the pNGB DM candidate, $m_V > 2m_\chi$ is assumed so that V decays. Perturbative unitarity is exploited to impose bounds on scalar and gauge couplings. Reference [112] considered three separate versions of the model, where the $U(1)_X$ is identified as $X = B - L$, $X = (B - L)_3$ acting only on the third generation, and finally $X = L_\mu - L_\tau$. In [113] the SM is extended with two complex scalar fields with different charges under the additional hidden $U(1)_X$ gauge group. WIMP-nucleon scattering proceeds via exchanges of the SM-like and two exotic Higgs bosons, and the predicted cross section is much smaller than the bounds from LZ. Indirect detection bounds from Fermi-LAT are exploited in order to constrain the parameter space of the theory from decays of the pNGB DM, which in general is unstable. Additionally, there exist studies where the model is embedded into a GUT setup based on $SO(10)$ [114, 115].

Other models

Pseudo-NGB DM has also been considered in models with two elementary Higgs fields [116], as motivated for instance by supersymmetric and axion theories. The Yukawa sector is not trivial due to the presence of two Higgs doublets: indeed four kinds of Yukawa couplings are discussed, with distinct consequences on the parameter space of the theory, but all of them being able to produce cancellations in direct detection. The subsequent phenomenological analysis is performed only through a selected type of Yukawas. The two doublets are rotated to the basis where couplings of one Higgs field match the couplings of the SM. Constraints from Higgs physics at LHC are implemented, together with indirect detection bounds from Fermi-LAT and MAGIC.

We finally mention the model presented in [117], where pNGB DM is obtained from a gauged $SU(2)_D$ symmetry, spontaneously broken to a global $U(1)_V$ when charged scalars acquire a non-vanishing vev. This model adds to the SM a complex doublet and a real triplet, charged under the new symmetry group. Depending on the chosen vacuum structure, we could get up to five Goldstone bosons. The authors illustrate the available potentials and their properties, depending on the presence of an explicit soft-breaking term. The scenario that guarantees the presence of pNGB DM is analyzed: its stability is ensured by the residual $U(1)_V$ symmetry. Recent results of the LZ experiment are used to constrain the model, finding that large regions of parameters that yield the thermal abundance remain viable at present.

Chapter 5

Muon collider phenomenology

In Chapter 2 we have discussed the current phenomenological constraints on pNGB DM, stressing that a wide region of parameter space with DM mass $m_\phi > m_h/2$ remains untested, as shown in Fig. 2.1. In this mass region, the most promising collider signal both at lepton and hadron machines is provided by VBF production through an off-shell Higgs, $VV \to h^* \to \phi\phi$, which is very challenging given its suppressed rate. Reference [40] has demonstrated, by considering a variety of existing and proposed collider projects, that only a muon collider (MC) can truly test pNGB DM. This is shown in the left panel of Fig. 5.1. In the same figure, we also show the reach on the marginal portal coupling

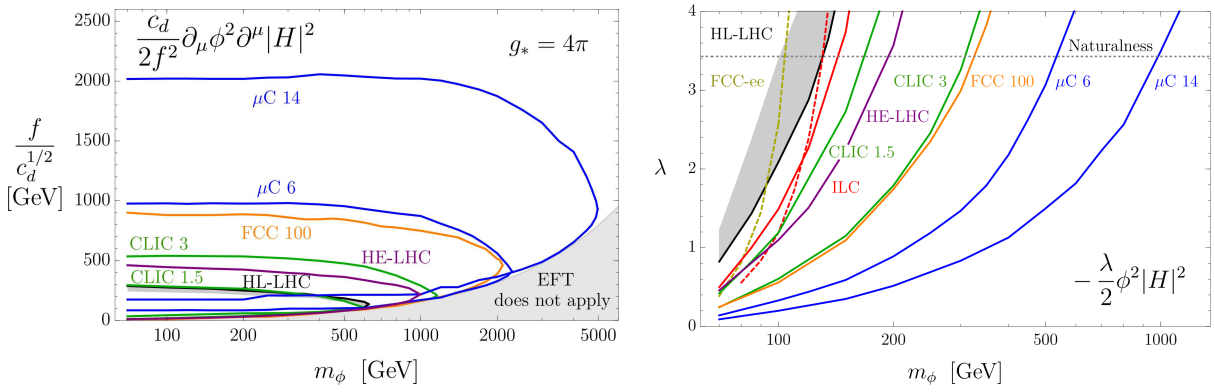

Figure 5.1: Projected reach of existing and future collider projects on the derivative Higgs portal (left) and marginal Higgs portal (right). Figures taken from [40].

λ. Although, as we saw in Fig. 2.3, this is now largely excluded as a thermal DM scenario, it is still interesting to consider the possibility that a new scalar ϕ exists, with a large coupling to the Higgs but no significant cosmological abundance today. For example, this is relevant in "neutral naturalness" solutions of the electroweak hierarchy problem, where ϕ corresponds to SM-neutral top partner scalars, as well as in models of electroweak baryogenesis; see [40, 118] and references therein. Therefore, in the following we also consider the marginal Higgs portal.

Figure 5.1 clearly shows the impressive estimated reach of a MC on both portals. There is, however, an important caveat. For the MC, the figure assumed [40] detector coverage up to $|\eta_\mu| = 6$ for the forward muons produced by the ZZ fusion signal

$$\mu^+\mu^- \to (h^* \to \phi\phi)\,\mu^+\mu^-\,, \tag{5.1}$$

where ϕ is assumed to be stable on the detector scale (the WW fusion process produces a completely invisible final state). However, since 2019 it has become clear that detecting forward particles at a MC detector would be a challenge. The reason is the need for shielding from the beam-induced background caused by beam muon decays, which in typical detector concepts limits the acceptance to particles with $\theta > 10^\circ$, or $|\eta| < 2.44$. This would essentially erase any hope to detect the signal in (5.1), since

the final state muons have typical pseudorapidities $|\eta_\mu|$ ranging from 4 to 6. This provides motivation to tackle an important and more general question: *what is the physics case in favor of the design and eventual construction of a dedicated forward muon detector at the MC?* In fact, since muons easily traverse the shielding material of the so-called "nozzles" that cover $|\eta| > 2.44$, detecting forward muons by means of standalone detectors may be technologically feasible.

In this chapter we begin to work on this question, by improving the sensitivity estimates shown in Fig. 5.1 to include more realistic accelerator and detector effects. These include: the unavoidable presence of a beam energy spread (BES); backgrounds including photons that are lost at $\theta < 10^o$, which were neglected in [40]; and a finite resolution on the energy measurement of the forward muons. After a few words of introduction to the MC in Section 5.1, as first physics case study we consider in Section 5.2 the signal of invisibly-decaying VBF-produced Higgs (i.e. Eq. (5.1) with on-shell h), estimating the reach on BR($h \to$ inv) as a function of the forward detector coverage and resolution. We then discuss the derivative and marginal Higgs portals in Section 5.3.

5.1 Introduction to muon colliders

Particle accelerators are a powerful and versatile approach to exploring physics beyond the SM. So far, two main types of circular colliders have been employed: e^+e^- and hadron machines. The former provide knowledge of the initial momenta and "clean" final states, but are limited in $\sqrt{s}$ by synchrotron radiation. The latter can more easily reach higher center of mass energies, but the longitudinal component of the momentum is unknown. Electron-positron colliders excel at precision measurements, whereas hadron colliders have historically played the role of discovery machines.

In the last few years, the idea of a circular $\mu^+\mu^-$ collider has gained significant traction [119–122]. A MC would combine the advantages of e^+e^- and hadronic machines: synchrotron radiation is strongly suppressed relative to electron-positron colliders, since $m_\mu/m_e \sim 200$; furthermore $\mu^+\mu^-$ collisions exploit the entire available collider energy, since the muon is an elementary particle, unlike the proton (and antiproton).

The fact that muons are unstable particles, with $\tau = 2.2$ μs at rest, poses great challenges to the realization of a MC. The decay of beam muons generates a large beam-induced background (BIB), whose effects have so far been best studied at $\sqrt{s} = 1.5$ TeV. With bunches of order 10^{12} muons at 750 GeV beam energy, $O(10^5)$ muon decays per meter are expected. To suppress the BIB the current MC detector design includes two tungsten nozzles for shielding, which as already mentioned limit the detector coverage to $|\eta| < 2.44$. As far as the center of mass energy is concerned, several benchmarks have been considered. The $\sqrt{s} = 3$ TeV option is often discussed for Higgs precision measurements, while higher energies of $6, 10, 14$, and 30 TeV have also been studied. Here we focus on a MC with center of mass energy and integrated luminosity

$$\sqrt{s} = 10 \text{ TeV} \qquad \text{and} \qquad L = 10 \text{ ab}^{-1} \,. \tag{5.2}$$

The extension to other energies is left for future work.

A high energy MC is essentially a collider of vector bosons, making it especially well suited to study Higgs-related processes like those of interest in this thesis. More generally, the reach of a high-energy MC compares favorably to that of a 100 TeV pp collider (FCC-hh), although exceptions exist, such as the production of particles that are subject only to QCD interactions. The physics case of a MC is extensive and covers a variety of BSM scenarios. We do not review it here, diving instead into the analysis of the first signal we study: the invisible decay of Higgs bosons produced in ZZ fusion.

5.2 Invisible Higgs decay

We begin by studying the process in (5.1) but with on-shell Higgs, which is very closely related (sharing in particular the same set of backgrounds) but simpler, in the sense that in the on-shell regime the signal kinematics do not depend on the type of portal considered. As a matter of fact the process is

only sensitive to BR($h \to$ inv). Deriving the first projected bounds on this quantity at the MC is the goal of this section.

With respect to the first study of DM pair production at the MC in [40], our analysis of the $\mu^+\mu^- \to \mu^+\mu^-$ + invisible final state includes several improvements:

1. We vary the maximum pseudorapidity at which the muons can be measured (fixed at $|\eta_\mu|_{\max} = 5$ or 6 in [40]) up to $|\eta_\mu|_{\max} = 10$, to better understand the acceptance requirements of the hypothetical forward muon detector.

2. We assume the muon beams to have an energy uncertainty of 0.1% [121], to which we refer as beam energy spread (BES).

3. We introduce a finite uncertainty on the energy measurement for the forward muons, considering 0.1% and 1% energy smearing (ES) in addition to the idealized case.

4. Finally, given the inclusion of more realistic accelerator/detector conditions we consider new backgrounds. We include the following processes:

   - $\mu^+\mu^- \to \mu^+\mu^-\bar{\nu}\nu$,
   - $\mu^+\mu^- \to \mu^+\mu^-$ (Bhabha scattering),
   - $\mu^+\mu^- \to \mu^+\mu^-\gamma$, if $|\eta_\gamma| > 2.5$,
   - $\mu^+\mu^- \to \mu^+\mu^-\gamma\gamma$, if $|\eta_\gamma| > 2.5$.

   Of these, only the first was accounted for in [40]. Photons are considered lost if they have $|\eta| > 2.5$ and therefore hit the BIB-shielding nozzles. As we are going to discuss, Bhabha scattering and the single-photon background become relevant here due to BES and ES, whereas the two-photon background is a priori relevant even in the idealized case, but was omitted in [40].

To simulate the signals and backgrounds we made use of the `MadGraph5_aMC@NLO` Monte Carlo generator [123], henceforth called `MadGraph` for short. For the $h \to$ invisible signal 100k events were generated, whereas 600k events were produced for each of the neutrino and Bhabha backgrounds, and finally 200k events for each of the lost photon backgrounds.

5.2.1 Accelerator and detector effects

Beam Energy Spread

To account for a 0.1% BES, we proceed as follows. For each `MadGraph` event, we randomly draw the energies E_i ($i = 1, 2$) from a normal distribution with mean $\sqrt{s}/2$ and standard deviation $10^{-3}\sqrt{s}/2$. In the laboratory frame (LAB) the four-momenta of the initial muons are then defined as

$$p_1^\mu = \left(E_1, 0, 0, \sqrt{E_1^2 - m_\mu^2}\right) , \qquad p_2^\mu = \left(E_2, 0, 0, -\sqrt{E_2^2 - m_\mu^2}\right) . \tag{5.3}$$

The `MadGraph` event is produced in the center of mass frame (COM) where the muons collide with equal energies and opposite three-momenta, therefore we find the longitudinal boost that takes us from LAB to COM,

$$(\Lambda^{\text{BES}})^\mu_\nu = \begin{pmatrix} \gamma & 0 & 0 & -\gamma v_z \\ 0 & 1 & 0 & 0 \\ 0 & 0 & 1 & 0 \\ -\gamma v_z & 0 & 0 & \gamma \end{pmatrix} , \quad \text{where} \quad v_z = \frac{\sqrt{E_1^2 - m_\mu^2} - \sqrt{E_2^2 - m_\mu^2}}{E_1 + E_2} , \tag{5.4}$$

while $\gamma = (1 - v_z^2)^{-1/2}$. Then, realistic events where BES is included are obtained by transforming the `MadGraph` momenta of all particles in the event back to the LAB, using the inverse boost $(\Lambda^{\text{BES}})^{-1} = \eta \cdot (\Lambda^{\text{BES}})^T \cdot \eta$.

Energy Smearing

For our exploratory investigation we consider, in addition to the idealized case without smearing of the final muon energies, the relative uncertainties $\sigma_E = 0.1\%$ and 1%. For each event, defining the four-momenta after the application of BES as $p_i^\mu = (E_i, \vec{p}_i)$, $i = 1, 2$, we draw the measured energy E_i' from a normal distribution with mean E_i and standard deviation $\sigma_E E_i$. The measured four-momentum becomes then

$$p_i'^\mu = \frac{E_i'}{E_i}\, p_i^\mu \,. \tag{5.5}$$

5.2.2 Analysis and BR($h \to$ inv) sensitivity

For illustration, in the analysis we consider four different scenarios:

- no BES and no ES (idealized),
- BES and no ES,
- BES and 0.1% ES,
- BES and 1% ES.

Monte Carlo events for the signal process $\mu^+\mu^- \to \mu^+\mu^- h$ are generated with `MadGraph`, imposing generation cuts on the maximum pseudorapidity of the muons, $|\eta_\mu| < 10$, and on their transverse momentum, $p_T^\mu > 10$ GeV. The same requirements are applied to background events; moreover, we require $|\eta_\gamma| > 2.5$ and $p_T^\gamma > 10$ GeV for the photons, to ensure they are outside the detector coverage.

Then, additional selection cuts on kinematic variables are applied in order to maximize the significance $\mathscr{S}$, defined as

$$\mathscr{S} = \frac{S}{\sqrt{S+B}} \,, \tag{5.6}$$

where S and B are the number of signal and background events after all cuts. Namely, calling $\sigma_{S,B}$ and $\epsilon_{S,B}$ the original Monte Carlo cross sections and the cut efficiencies, we have $S = \sigma_S \epsilon_S L$ and $B = \sigma_B \epsilon_B L$, with L the integrated luminosity. The maximization of the significance is performed by selecting specific intervals of the following kinetic variables: the missing invariant mass (MIM), the missing transverse energy (MET or $\not{E}_T$), the pseudorapidity separation among the muons ($\Delta\eta_{\mu\mu}$) and the invariant mass of the muons ($M_{\mu\mu}$). Calling p_{μ^+}, p_{μ^-} the four-momenta of the final-state muons, we define the missing four-momentum as

$$\not{p} = (\sqrt{s}, \vec{0}\,) - p_{\mu^+} - p_{\mu^-} \,. \tag{5.7}$$

Thus the kinematic variables are taken to be ($M_{\mu\mu}$ is defined in the standard way)

$$\text{MIM} \equiv (\not{p}_\alpha \not{p}^\alpha)^{1/2} \,, \qquad \not{E}_T \equiv (\not{p}_x^2 + \not{p}_y^2)^{1/2} \,, \qquad \Delta\eta_{\mu\mu} \equiv |\eta_{\mu^+} - \eta_{\mu^-}| \,. \tag{5.8}$$

We find that the combination of BES and ES only has important effects on the MIM distribution, while the $\not{E}_T$, $\Delta\eta_{\mu\mu}$ and $M_{\mu\mu}$ distributions remain essentially unchanged. In Fig. 5.2 we report the latter three (choosing, for definiteness, the idealized case). On the other hand, the impact of BES and ES on the MIM can be observed in Fig. 5.3, which deserves a detailed discussion. The most important effect regards the $\mu^+\mu^-\gamma$ background: while in the idealized case one has $\not{p} = p_\gamma$ and therefore MIM $= 0$, the inclusion of BES spreads out the MIM distribution up to values of several hundreds GeV; including a 1% ES increases the effect further. Thus, the single-photon background now plays an important role in the signal region MIM $\approx m_h$. The distribution for Bhabha scattering is also smeared, but in a less dramatic fashion (in any case, Bhabha can be efficiently suppressed with a MET cut). For the neutrino background, we observe that the $Z \to \bar{\nu}\nu$ peak is washed away. Adding on top of this a 0.1% ES does not cause large modifications, while a 1% ES renders the distribution extremely broad. For the signal, we observe that the 125 GeV peak is progressively broadened by the inclusion of realistic effects. Qualitatively, we can say that the BES is the dominant effect if 0.1% ES is assumed, while it becomes less important than ES if the latter is set to 1%.

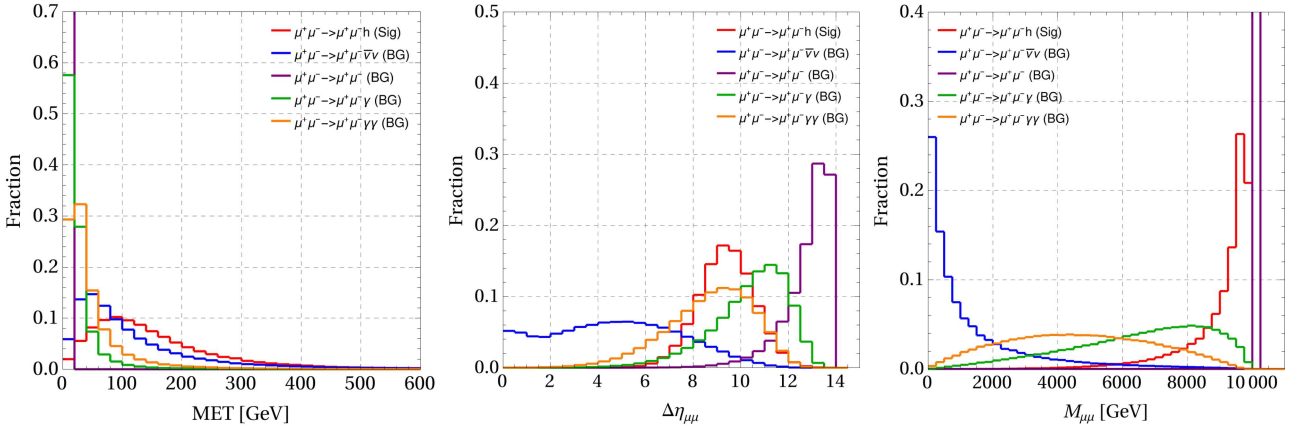

Figure 5.2: $\not{E}_T$ (*left*), $\Delta\eta_{\mu\mu}$ (*center*), and $M_{\mu\mu}$ (*right*) distributions for the $\mu^+\mu^-h$ signal and the four backgrounds, in the idealized scenario. These distributions are very little affected by the application of BES and ES.

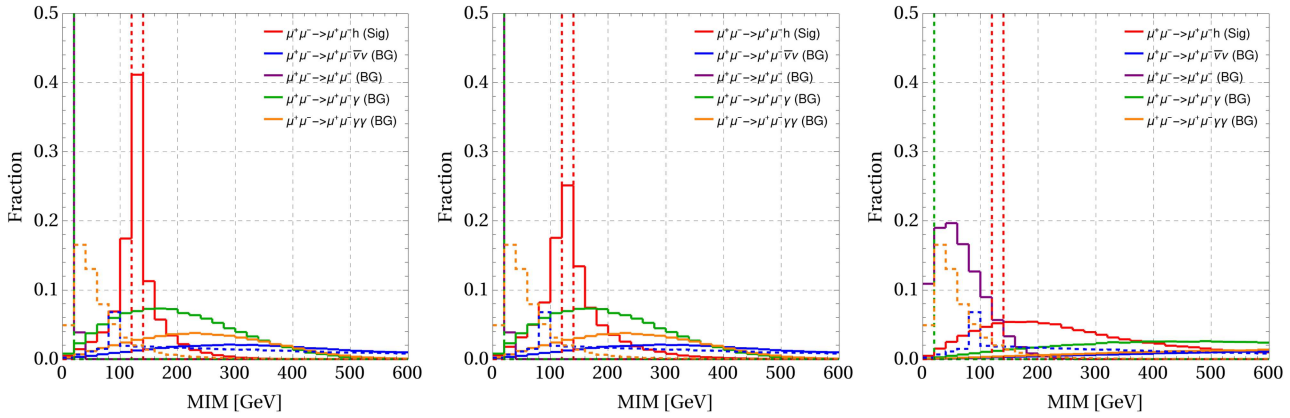

Figure 5.3: MIM distributions for the $\mu^+\mu^-h$ signal and the four backgrounds, before (dashed lines) and after (solid lines) the application of 0.1% BES combined with: no ES (*left*); 0.1% ES (*center*); and 1% ES (*right*).

Cut-flow	$\mu^+\mu^-h$	$\mu^+\mu^-\bar{\nu}\nu$	$\mu^+\mu^-$	$\mu^+\mu^-\gamma$	$\mu^+\mu^-\gamma\gamma$
0.1% BES, no ES					
Generation cuts	84.8	1460	$2.79 \cdot 10^6$	14100	146
100 GeV < MIM < 150 GeV	55.4	60.4	0	3360	15.5
$\Delta\eta_{\mu\mu} > 7$	54.4	38.1	0	3250	13.2
$\not{E}_T > 60$ GeV	45.5	19.4	0	181	2.30
$M_{\mu\mu} > 9500$ GeV	30.6	0.102	0	0.0703	0
0.1% BES + 1% ES					
Generation cuts	84.8	1460	$2.76 \cdot 10^6$	14000	146
MIM < 600 GeV	76.7	261	$2.76 \cdot 10^6$	7900	33.9
$\Delta\eta_{\mu\mu} > 7$	75.1	109	$2.75 \cdot 10^6$	7600	28.3
$\not{E}_T > 90$ GeV	51.7	31.1	0	156	2.20
$M_{\mu\mu} > 9250$ GeV	34.3	0.661	0	0.984	0

Table 5.1: Cross sections for the $\mu^+\mu^-h$ signal and the four backgrounds, expressed in femtobarn. The "Generation cuts" line reports the `MadGraph` cross section, with $\sqrt{s} = 10$ TeV, $|\eta_\mu| < 10$, $p_T^\mu > 10$ GeV, as well as $|\eta_\gamma| > 2.5$, $p_T^\gamma > 10$ GeV for photon backgrounds. The following lines present the residual cross sections after each kinematic cut is applied. We report scenarios with 0.1% BES combined with: no ES (top) and 1% ES (bottom). The signal cross sections correspond to BR($h \to$ inv) = 1.

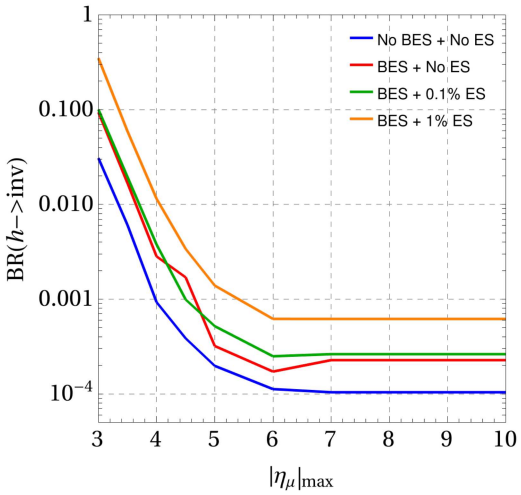

Figure 5.4: Projected 95% CL bounds on BR($h \to$ inv) at a $\sqrt{s} = 10$ TeV muon collider with $L = 10$ ab^{-1} luminosity. All four scenarios are reported: the idealized case (blue), 0.1% BES and no ES (red), 0.1% BES and 0.1% ES (green) and 0.1% BES and 1% ES (orange).

The fact that the MIM distribution drastically changes from one scenario to another is reflected in our event selection: in Table 5.1 we report the optimized cuts when the BES is combined with no ES and with 1% ES, since these two scenarios are largely different. One sees that the cut on the MIM changes much more than those on the remaining variables. The Bhabha scattering background has a very large cross section at generation level, but is efficiently removed already by the MIM cut if no ES is present, or by the $\not{E}_T$ cut for 1% ES. The final requirement on $M_{\mu\mu}$ is also useful to maximize the significance.

Finally, we calculate the expected 95% CL bound on BR($h \to$ inv) by requiring $\mathscr{S} = 1.64$, where the significance $\mathscr{S}$ was defined in Eq. (5.6). Again, recall that we assume an integrated luminosity $L = 10$ ab^{-1}. To verify how the sensitivity evolves with the angular coverage of the forward detector, the calculations are repeated for values of $|\eta_\mu|_{\max}$ between 3 and 10. The final result is reported in Fig. 5.4. The figure confirms that BES is the dominant effect for 0.1% ES, as seen from the proximity of the red and green curves. On the other hand, for 1% ES the sensitivity is appreciably reduced, but it still reaches BR($h \to$ inv) $\approx 6 \times 10^{-4}$. This is a very strong reach, better than the SM prediction for the $h \to 4\nu$ branching ratio. In addition, we see that the sensitivity reaches an asymptotic value for $|\eta_\mu|_{\max} \geq 6$, meaning that a larger detector coverage would not be required. Conversely, the bounds starkly deteriorate as the maximum pseudorapidity is progressively reduced from 6 to 3.

5.3 Pair production of invisible scalars

This section is devoted to the signal in Eq. (5.1). We consider the two Higgs portals, derivative and marginal, separately, since now the kinematics are significantly different, as can be gleaned from the different energy behaviors of the partonic cross sections in Eqs. (2.15) and (2.30). The analysis is very similar to the one presented in Section 5.2 for invisible Higgs decays: we assume the same benchmarks for the BES and ES effects, and include the same four backgrounds. We fix $|\eta_\mu|_{\max} = 10$ (which, based on Fig. 5.4, we expect to give very similar results to $|\eta_\mu|_{\max} = 6$). Signal events are generated for DM masses between $m_\phi = 70$ GeV and $m_\phi = 1000$ GeV. For each of the signal processes, 100k Monte Carlo events were generated, whereas 200k events were used for each of the backgrounds.

5.3.1 Derivative portal

We generate signal events by setting the coupling $f/c_d^{1/2} = 1$ TeV, while imposing generation cuts on the pseudorapidity, $|\eta_\mu| < 10$, and transverse momenta, $p_T^\mu > 10$ GeV, of the muons. Since in the $h \to$ invisible analysis we have found that the MIM is the most affected variable when moving from

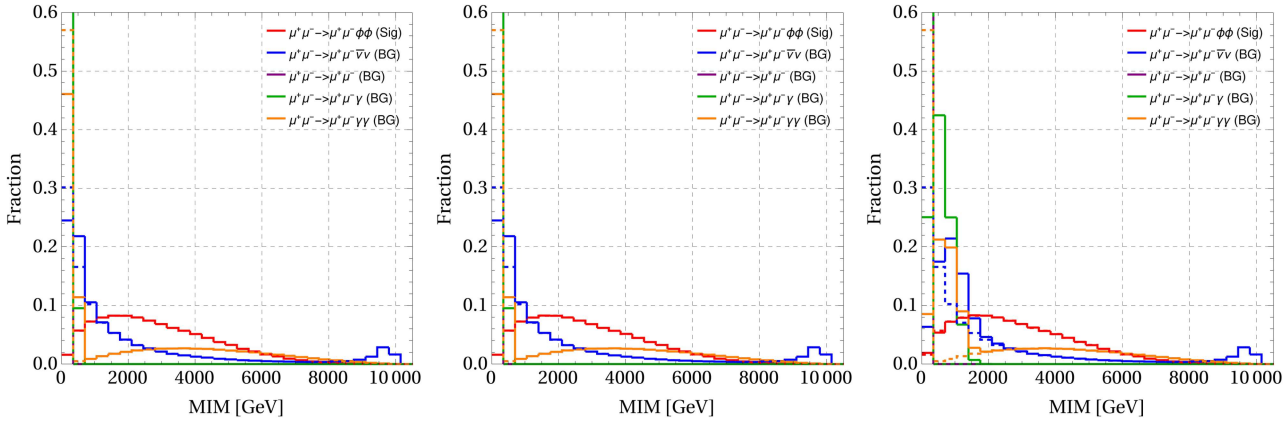

Figure 5.5: MIM distributions for the $\mu^+\mu^-(h^* \to \phi\phi)$ signal with $m_\phi = 100$ GeV, mediated by the derivative portal, and the four backgrounds, before (dashed lines) and after (solid lines) the application of 0.1% BES combined with no ES (*left*), 0.1% ES (*center*) and 1% ES (*right*).

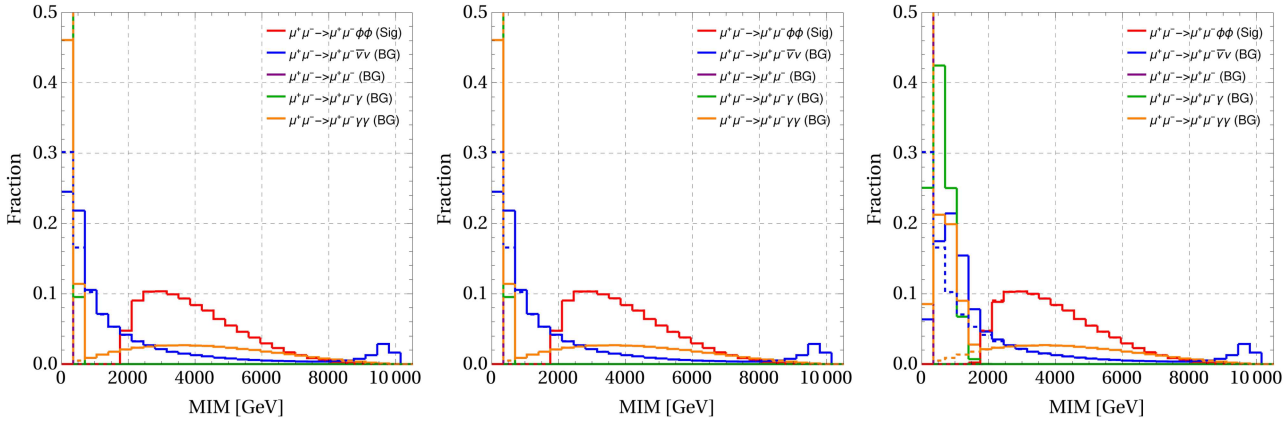

Figure 5.6: MIM distributions for the $\mu^+\mu^-(h^* \to \phi\phi)$ signal with $m_\phi = 900$ GeV, mediated by the derivative portal, and the four backgrounds, before (dashed lines) and after (solid lines) the application of 0.1% BES combined with no ES (*left*), 0.1% ES (*center*) and 1% ES (*right*).

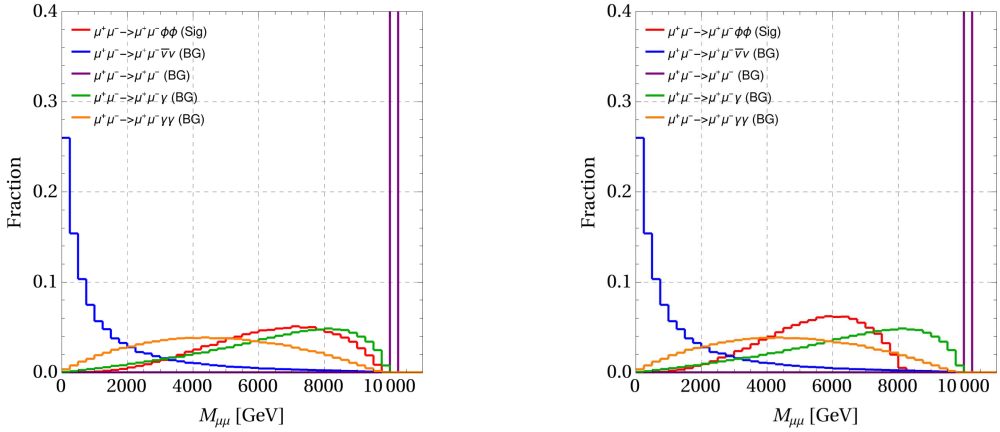

Figure 5.7: $M_{\mu\mu}$ distributions for the four backgrounds and the $\mu^+\mu^-(h^* \to \phi\phi)$ signal mediated by the derivative portal with $m_\phi = 100$ GeV (*left*) and $m_\phi = 900$ GeV (*right*), in the idealized scenario. These distributions are not significantly affected by the inclusion of BES and ES.

the idealized limit to a more realistic setup, here too we begin by looking at the MIM distributions. Figure 5.5 reports them for $m_\phi = 100$ GeV. The signal distribution is very broad as a consequence of the energy dependence of the partonic cross section, as already noted in [40]. All distributions,

for signal and backgrounds, have significant support at low MIM; conversely, for MIM $\gtrsim$ 2000 GeV the neutrino and two-photon backgrounds remain significant, along with the signal. This is already an interesting finding, since the two-photon background was neglected in [40]. In Fig. 5.6 we show the MIM distributions for $m_\phi = 900$ GeV. Here, since the signal satisfies MIM > 1800 GeV, the overlap with backgrounds at low MIM is automatically avoided, even for 1% ES. It is also useful to check the $M_{\mu\mu}$ distributions, shown in Fig. 5.7 for the two benchmark DM masses considered. These distributions are not significantly affected by the inclusion of BES and ES, therefore we show them in the idealized limit. We see that the signal $M_{\mu\mu}$ distribution is broad, with shape rather similar to the single- and two-photon backgrounds.

Cut-flow	$\mu^+\mu^-\phi\phi$	$\mu^+\mu^-\bar{\nu}\nu$	$\mu^+\mu^-$	$\mu^+\mu^-\gamma$	$\mu^+\mu^-\gamma\gamma$
0.1% BES, no ES					
Generation cuts	0.0687	1460	$2.79 \cdot 10^6$	14100	146
600 GeV < MIM < 8000 GeV	0.0647	726	0	0	59.7
$\Delta\eta_{\mu\mu} > 8$	0.0488	6.03	0	0	40.4
$\not{E}_T > 80$ GeV	0.0308	0.729	0	0	2.14
$M_{\mu\mu} > 5500$ GeV	0.0243	0.277	0	0	0.839
0.1% BES + 1% ES					
Generation cuts	0.0686	1460	$2.75 \cdot 10^6$	14000	146
1500 GeV < MIM < 8000 GeV	0.0514	422	0	39.8	56.0
$\Delta\eta_{\mu\mu} > 8$	0.0377	2.21	0	32.1	38.9
$\not{E}_T > 80$ GeV	0.0228	0.314	0	0.562	2.10
$M_{\mu\mu} > 5600$ GeV	0.0160	0.0583	0	0	0.737

Table 5.2: Cross sections for the $\mu^+\mu^-(h^* \to \phi\phi)$ signal mediated by the derivative portal and the four backgrounds, expressed in femtobarn, for $m_\phi = 100$ GeV. The "Generation cuts" line reports the `MadGraph` cross section, with $\sqrt{s} = 10$ TeV, $|\eta_\mu| < 10$, $p_T^\mu > 10$ GeV, as well as $|\eta_\gamma| > 2.5$, $p_T^\gamma > 10$ GeV for photon backgrounds. The following lines present the residual cross sections after each kinematic cut is applied. We report scenarios with 0.1% BES combined with: no ES (top) and 1% ES (bottom). The signal cross sections correspond to $f/c_d^{1/2} = 1$ TeV.

Cut-flow	$\mu^+\mu^-\phi\phi$	$\mu^+\mu^-\bar{\nu}\nu$	$\mu^+\mu^-$	$\mu^+\mu^-\gamma$	$\mu^+\mu^-\gamma\gamma$
0.1% BES, no ES					
Generation cuts	0.0365	1460	$2.79 \cdot 10^6$	14100	146
2000 GeV < MIM < 8000 GeV	0.0353	292	0	0	51.4
$\Delta\eta_{\mu\mu} > 8$	0.0251	0.182	0	0	36.2
$\not{E}_T > 80$ GeV	0.0145	0.0292	0	0	1.97
$M_{\mu\mu} > 4300$ GeV	0.0127	0.0292	0	0	1.22
0.1% BES + 1% ES					
Generation cuts	0.0365	1460	$2.75 \cdot 10^6$	14000	146
2000 GeV < MIM < 8000 GeV	0.0352	299	0	0.0703	51.4
$\Delta\eta_{\mu\mu} > 8$	0.0250	0.204	0	0.0703	36.1
$\not{E}_T > 80$ GeV	0.0144	0.0292	0	0	1.96
$M_{\mu\mu} > 4200$ GeV	0.0128	0.0292	0	0	1.27

Table 5.3: Cross sections for the $\mu^+\mu^-(h^* \to \phi\phi)$ signal mediated by the derivative portal and the four backgrounds, expressed in femtobarn, for $m_\phi = 900$ GeV. The "Generation cuts" line reports the `MadGraph` cross section, with $\sqrt{s} = 10$ TeV, $|\eta_\mu| < 10$, $p_T^\mu > 10$ GeV, as well as $|\eta_\gamma| > 2.5$, $p_T^\gamma > 10$ GeV for photon backgrounds. The following lines present the residual cross sections after each kinematic cut is applied. We report scenarios with 0.1% BES combined with: no ES (top) and 1% ES (bottom). The signal cross sections correspond to $f/c_d^{1/2} = 1$ TeV.

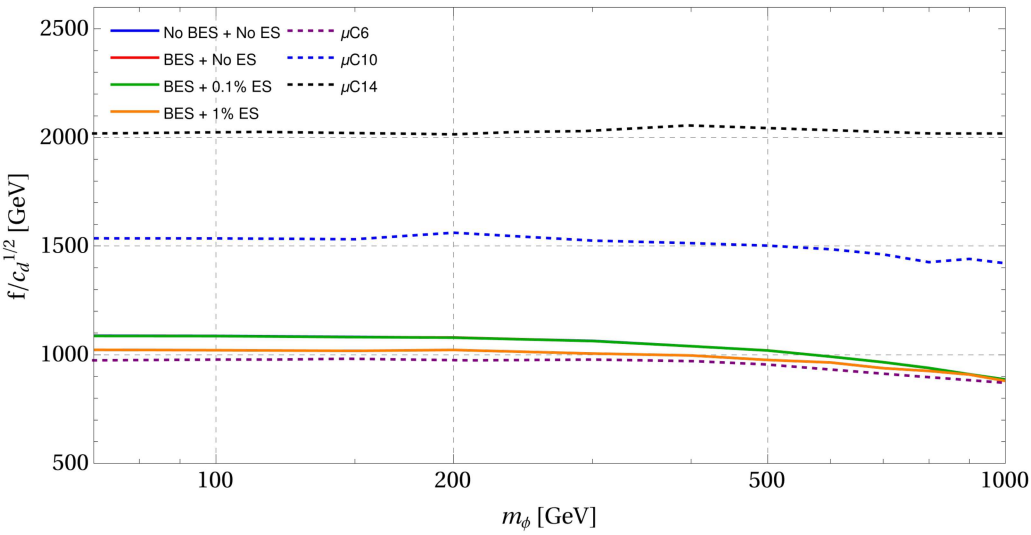

Figure 5.8: Sensitivity to the scale $f/c_d^{1/2}$ parametrizing the dimension-6 derivative Higgs portal, for a $\sqrt{s} = 10$ TeV muon collider with $L = 10$ ab^{-1} integrated luminosity. Dashed lines are obtained in the idealized scenario and considering only the neutrino background $\mu^+\mu^-\bar{\nu}\nu$: we have calculated the $\sqrt{s} = 10$ TeV line, whereas the 6 TeV and 14 TeV lines were taken from [40]. Solid lines correspond to the four standard scenarios considered in this thesis. Notice that the solid blue, red, and green lines are superimposed.

The cut-flows for $m_\phi = 100$ GeV and $m_\phi = 900$ GeV are shown in Tables 5.2 and 5.3, respectively. For $m_\phi = 100$ GeV we notice that the lower MIM cut is strongly increased when going from the scenario without ES to the one with 1% ES, which is explained by the previous discussion and by Fig. 5.5. This does not happen for $m_\phi = 900$ GeV, where the maximal sensitivity is obtained with the same MIM cut regardless of the assumed ES. At the end of the selection, the $\gamma\gamma$ background turns out to be largest, since its MIM distribution is spread out over a very wide range. On the other hand, the single-γ process is efficiently removed, along with the Bhabha scattering. Finally, we comment on $M_{\mu\mu}$: given the distributions in Fig. 5.7, a more stringent cut on this variable (as applied previously in the $h \to$ inv analysis) is not beneficial, since it leads to a too strong suppression of the signal.

Finally, we extract the bounds on $f/c_d^{1/2}$ by rescaling the signal rate with c_d^2/f^4 (at fixed m_ϕ) and requiring the significance to be $\mathscr{S} = 1.64$. The results are presented in Fig. 5.8. The dashed blue line shows the sensitivity of a $\sqrt{s} = 10$ TeV MC in the idealized limit, *and considering only the neutrino background*. This can be fairly compared to, and appears to be consistent with, the $\sqrt{s} = 6$ and 14 TeV lines (dashed purple and dashed black, respectively) which were taken from [40]. The solid blue line (coinciding with the solid green line, and also with the red solid one) differs from the dashed blue line only for the inclusion of the $\gamma\gamma$ background, which we therefore find to have significant impact. In the future, it will be interesting to study further approaches to suppress this background. The additional inclusion of BES and ES has negligible or small effect.

5.3.2 Marginal portal

For the marginal Higgs portal, we generate signal events by setting the coupling $\lambda = 1$ and imposing generation cuts on the pseudorapidity, $|\eta_\mu| < 10$, and transverse momenta, $p_T^\mu > 10$ GeV, of the muons. As we did for the derivative portal, we take $m_\phi = 100$ GeV and $m_\phi = 900$ GeV as illustrative benchmarks. The corresponding MIM distributions are shown in Figures 5.9 and 5.10, respectively. The first, general feature we note is that the signal has a different shape compared to the derivative portal, with a sharp peak at MIM $= 2m_\phi$ in the idealized case. Again, we observe that a 0.1% (1%) ES is less (more) important than the BES. Comparing the two figures we learn that, while for $m_\phi = 100$ GeV the background shapes resemble the one of the signal after BES and ES are introduced, for $m_\phi = 900$ GeV a better separation is obtained. We also show in Fig. 5.11 the $M_{\mu\mu}$ distributions, where the signal shows a sharper feature compared to the derivative portal.

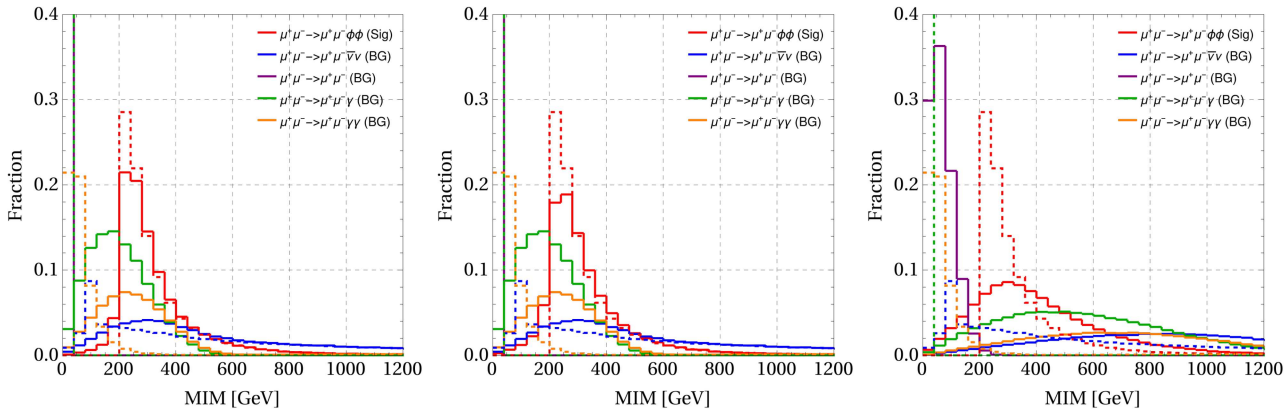

Figure 5.9: MIM distributions for the $\mu^+\mu^-(h^* \to \phi\phi)$ signal with $m_\phi = 100$ GeV, mediated by the marginal Higgs portal, and the four backgrounds, before (dashed lines) and after (solid lines) the application of 0.1% BES combined with no ES (*left*), 0.1% ES (*center*) and 1% ES (*right*).

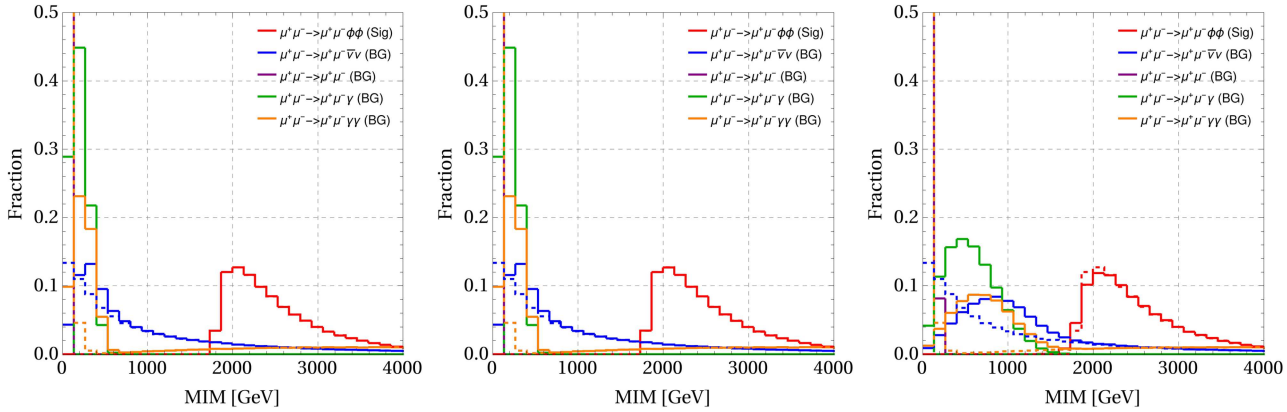

Figure 5.10: MIM distributions for the $\mu^+\mu^-(h^* \to \phi\phi)$ signal with $m_\phi = 900$ GeV, mediated by the marginal Higgs portal, and the four backgrounds, before (dashed lines) and after (solid lines) the application of 0.1% BES combined with no ES (*left*), 0.1% ES (*center*) and 1% ES (*right*).

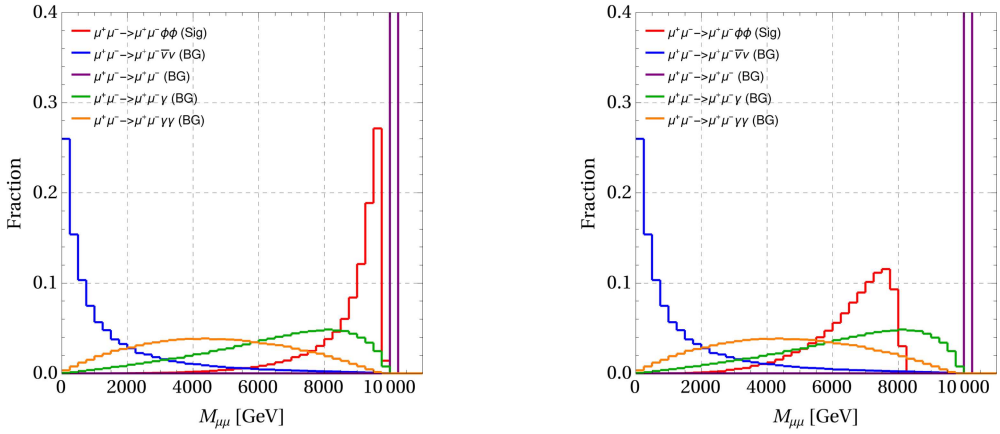

Figure 5.11: $M_{\mu\mu}$ distributions for the four backgrounds and the $\mu^+\mu^-(h^* \to \phi\phi)$ signal mediated by the marginal portal with $m_\phi = 100$ GeV (*left*) and $m_\phi = 900$ GeV (*right*), in the idealized scenario. These distributions are not significantly affected by the inclusion of BES and ES.

Cut-flow	$\mu^+\mu^-\phi\phi$	$\mu^+\mu^-\bar{\nu}\nu$	$\mu^+\mu^-$	$\mu^+\mu^-\gamma$	$\mu^+\mu^-\gamma\gamma$
0.1% BES, no ES					
Generation cuts	0.306	1460	$2.79 \cdot 10^6$	14100	146
200 GeV < MIM < 600 GeV	0.264	434	0	3800	36.9
$\Delta\eta_{\mu\mu} > 8$	0.230	100	0	3410	25.3
$\not{E}_T > 80$ GeV	0.168	22.1	0	104	1.86
$M_{\mu\mu} > 8500$ GeV	0.136	0.328	0	0.0703	0.000732
0.1% BES + 1% ES					
Generation cuts	0.305	1460	$2.75 \cdot 10^6$	14000	146
100 GeV < MIM < 800 GeV	0.270	429	$5.77 \cdot 10^5$	10500	52.0
$\Delta\eta_{\mu\mu} > 8$	0.236	106	$5.75 \cdot 10^5$	9620	36.0
$\not{E}_T > 80$ GeV	0.172	27.8	0	215	2.63
$M_{\mu\mu} > 9400$ GeV	0.0714	0.394	0	0.281	0

Table 5.4: Cross sections for the $\mu^+\mu^-(h^* \to \phi\phi)$ signal mediated by the marginal portal and the backgrounds, expressed in femtobarn, for $m_\phi = 100$ GeV. The "Generation cuts" line reports the `MadGraph` cross section, with $\sqrt{s} = 10$ TeV, $|\eta_\mu| < 10$, $p_T^\mu > 10$ GeV, as well as $|\eta_\gamma| > 2.5$, $p_T^\gamma > 10$ GeV for photon backgrounds. The following lines present the residual cross sections after each kinematic cut is applied. We report scenarios with 0.1% BES combined with: no ES (top) and 1% ES (bottom). The signal cross sections correspond to $\lambda = 1$.

Cut-flow	$\mu^+\mu^-\phi\phi$	$\mu^+\mu^-\bar{\nu}\nu$	$\mu^+\mu^-$	$\mu^+\mu^-\gamma$	$\mu^+\mu^-\gamma\gamma$
0.1% BES, no ES					
Generation cuts	$0.449 \cdot 10^{-3}$	1460	$2.79 \cdot 10^6$	14100	146
1800 GeV < MIM < 3000 GeV	$0.351 \cdot 10^{-3}$	156	0	0	11.9
$\Delta\eta_{\mu\mu} > 8$	$0.276 \cdot 10^{-3}$	0.102	0	0	7.83
$\not{E}_T > 95$ GeV	$0.159 \cdot 10^{-3}$	0.0219	0	0	0.299
$M_{\mu\mu} > 4600$ GeV	$0.155 \cdot 10^{-3}$	0.0219	0	0	0.262
0.1% BES + 1% ES					
Generation cuts	$0.449 \cdot 10^{-3}$	1460	$2.75 \cdot 10^6$	14000	146
1800 GeV < MIM < 3000 GeV	$0.338 \cdot 10^{-3}$	165	0	1.19	11.9
$\Delta\eta_{\mu\mu} > 8$	$0.267 \cdot 10^{-3}$	0.168	0	0.843	7.83
$\not{E}_T > 95$ GeV	$0.153 \cdot 10^{-3}$	0.0437	0	0.0703	0.294
$M_{\mu\mu} > 4600$ GeV	$0.150 \cdot 10^{-3}$	0.0365	0	0	0.258

Table 5.5: Cross sections for the $\mu^+\mu^-(h^* \to \phi\phi)$ signal mediated by the marginal portal and the backgrounds, expressed in femtobarn, for $m_\phi = 900$ GeV. The "Generation cuts" line reports the `MadGraph` cross section, with $\sqrt{s} = 10$ TeV, $|\eta_\mu| < 10$, $p_T^\mu > 10$ GeV, as well as $|\eta_\gamma| > 2.5$, $p_T^\gamma > 10$ GeV for photon backgrounds. The following lines present the residual cross sections after each kinematic cut is applied. We report scenarios with 0.1% BES combined with: no ES (top) and 1% ES (bottom). The signal cross sections correspond to $\lambda = 1$.

The cut-flows are reported in Tables 5.4 and 5.5. For $m_\phi = 100$ GeV the single-γ background cannot be completely removed, although it is significantly reduced by a hard $M_{\mu\mu}$ cut (which is also able to render negligible the $\gamma\gamma$ process), but remains subleading to the neutrino background. Conversely, for $m_\phi = 900$ GeV we can completely remove the single-photon contribution, but the two-photon background remains sizable and dominates over the neutrino background. This happens because, in view of the distributions shown in the right panel of Fig. 5.11, we cannot afford a hard cut on $M_{\mu\mu}$, which would eliminate the $\gamma\gamma$ contribution but also suppress the signal too much.

Finally, we derive 95% CL bounds on the portal coupling, by accounting for the scaling of the signal cross section with λ^2. The projected sensitivity in the (m_ϕ, λ) parameter space is shown in Fig. 5.12. First, we compare the results in the idealized case. If only the neutrino background is included (dashed blue line), the sensitivity is found to be consistent with previous results at $\sqrt{s} = 6$ and 14 TeV [40].

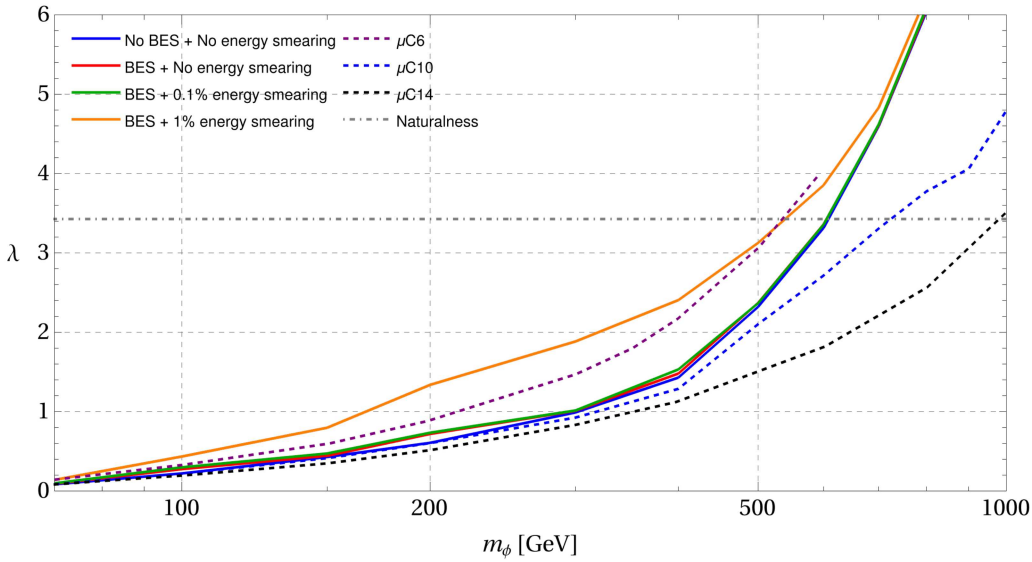

Figure 5.12: Sensitivity to the renormalizable Higgs portal coupling λ, for a $\sqrt{s} = 10$ TeV muon collider with $L = 10$ ab^{-1} integrated luminosity. Dashed lines are obtained in the idealized scenario and considering only the neutrino background $\mu^+\mu^-\bar{\nu}\nu$: we have calculated the $\sqrt{s} = 10$ TeV line, whereas the 6 TeV and 14 TeV lines were taken from [40]. Solid lines correspond to the four standard scenarios considered in this thesis. The dot-dashed grey line labeled "naturalness" indicates the coupling strength corresponding to ϕ playing the role of scalar top partners, namely $\lambda = \sqrt{4N_c}\, y_t^2 \approx 3.4$ [40, 118].

Comparing this with our idealized result including the $\gamma\gamma$ background (solid blue), we find good agreement at low masses, 70 GeV $\lesssim m_\phi \lesssim$ 300 GeV. This is consistent with our previous discussion and with Table 5.4, where we saw that the two-photon background could be efficiently suppressed to a subleading level with respect to $\mu^+\mu^-\bar{\nu}\nu$. Conversely, for $m_\phi \gtrsim 300$ GeV the solid and dashed blue lines become separated, since the suppression of the $\gamma\gamma$ contribution becomes inefficient and this background dominates over the neutrino one, as already seen in Table 5.5.

When accelerator and detector effects are included (solid lines in Fig. 5.12), we observe that up to 0.1% ES the results do not differ significantly from the idealized scenario. The situation is different if 1% ES is assumed: the sensitivity on λ is worsened for $m_\phi \lesssim 700$ GeV, whereas for heavier ϕ the MIM distribution comes to the rescue, and even BES + 1% ES do not affect strongly the expected sensitivity.

Chapter 6

Conclusions

In this thesis we discussed different aspects of pNGB DM, a thermal candidate characterized by a momentum-dependent interaction with the SM, which automatically suppresses its scattering on nuclei. This removes the tension with direct detection experiments that many other WIMP models are experiencing. Beyond this phenomenological argument, pNGB DM has important ultraviolet motivations, especially from extended composite Higgs models where the Higgs and DM fields arise together as pseudo-Goldstone bosons.

In Chapter 1 we gave a brief introduction to DM, recalling part of its history and the evidences that point to its presence in the Universe, as well as the properties that DM needs to have in order to satisfy experimental constraints. We focused on thermal candidates, providing a derivation of the freeze-out mechanism which sets the relic abundance, and showing how the WIMP miracle arises. Chapter 2 introduced the main phenomenological aspects of pNGB DM, which stem from the derivative Higgs portal. We reviewed the existing constraints from the DM relic abundance, invisible Higgs decays, and indirect detection experiments. As a useful comparison we also presented the marginal or renormalizable Higgs portal, which has a long history as a minimal DM scenario. Since this portal does not lead to a suppression of the DM-nucleon scattering rate, it is by now mostly excluded by data: we have shown the most up to date constraints, which bound $m_\phi > 2.8$ TeV. Nonetheless, going beyond the DM motivation, a marginal Higgs portal to invisible scalars remains a very interesting possibility for physics BSM.

We dedicated the central part of the thesis to review the existing proposals of pNGB DM models, identifying two large classes of theories. The first one, exposed in Chapter 3, encompasses composite models where both the DM and the Higgs are pNGBs. We briefly sketched the basic ingredients of composite Higgs models and described the minimal symmetry pattern that allows the realization of composite Higgs and pNGB DM, namely the $SO(6)/SO(5)$ coset. We then collected the relevant references. The second class, presented in Chapter 4, consists of scalar extensions of the SM where the DM arises as a pNGB but the Higgs does not, hence the hierarchy problem is not addressed. Here the suppression of direct detection is obtained for specific choices of the explicit global symmetry breaking terms. We made an explicit example based on an extension of the SM by a single complex scalar field, discussing the interplay with Higgs couplings measurements. Finally, we reviewed the existing literature in this class.

Chapter 5 represents the original part of this thesis. In the previous study [40], a muon collider was found to be the only future accelerator project option with real capability to test pNGB DM ϕ in the currently wide-open mass region $m_\phi > m_h/2$, exploiting the ZZ fusion process $\mu^+\mu^- \to \mu^+\mu^-(h^* \to \phi\phi)$. However, the final state muons produced in this process are extremely forward. This clashes with the shielding requirements that MC detectors need to deploy against the beam-induced background, limiting the acceptance to $|\eta| < 2.5$. Starting from these observations, here we began to build the physics case to install a dedicated muon detector in the far forward regions around the MC interaction point. We took the maximum angular coverage of such a detector as a varying

parameter, and accounted for more realistic effects compared to [40]. These include the beam energy spread and a finite resolution for the measurement of the energies of the forward muons. We focused our study on a $\sqrt{s} = 10$ TeV muon collider.

Firstly, we estimated the sensitivity on the branching ratio for $h \to$ invisible, a closely related signal where the Higgs is produced on-shell. We found that the optimal angular coverage would be $|\eta_\mu|_{\max} = 6$, with rapid degradation if this value is decreased. The effects of the BES and ES were found to be important: while in the idealized case we estimated a 95% CL sensitivity BR($h \to$ inv) $= 10^{-4}$, including the BES and a 1% ES gives 6×10^{-4}. For context, the current bound from ATLAS is 0.11, whereas FCC-hh is expected to reach 2.5×10^{-4}. Thus, the results of our initial study are certainly encouraging.

Then, we studied the sensitivity to the pair production of invisible ϕ scalars in ZZ fusion, now mediated by an off-shell Higgs. We considered both the derivative and marginal portals, varying m_ϕ between 70 GeV and 1 TeV.

For the derivative portal, we found that even in the idealized limit the inclusion of the two-photon background leads to a weaker sensitivity than obtained in [40], where backgrounds including lost photons were not considered. On the other hand, the inclusion of BES and ES has little additional effect. In the future, it will be important to look for other kinematic variables that can help suppress the $\mu^+\mu^-\gamma\gamma$ background.

For the marginal portal, in the idealized limit we found that the two-photon background can be efficiently suppressed for $m_\phi \lesssim 300$ GeV, but for larger masses it is important and leads to a sensitivity degradation compared to the results of [40] where only the neutrino background was considered. When including BES and ES, we observe stronger effects than in the case of the derivative portal, with a weakening of the projected bound on λ for $m_\phi \lesssim 700$ GeV, if the ES is set to 1%.

This thesis lays a foundation for many future investigations. Aspects deserving further work include: the already-mentioned search for kinematic variables that can efficiently suppress the backgrounds containing lost photons; a better treatment of photon radiation, going beyond the baseline approximations made here; the extension of our study to larger values of the ES, such as 10%; and the analysis of other MC center of mass energies, including the commonly discussed $\sqrt{s} = 3$ TeV as well as values above 10 TeV.

Bibliography

[1] J. H. Oort. "The force exerted by the stellar system in the direction perpendicular to the galactic plane and some related problems". In: *Bulletin of the Astronomical Institutes of The Netherlands* 6 (Aug. 1932). URL: https://ui.adsabs.harvard.edu/abs/1932BAN.....6..2490.

[2] H. Andernach and F. Zwicky. "English and Spanish Translation of Zwicky's (1933) The Redshift of Extragalactic Nebulae". (2017). URL: https://arxiv.org/abs/1711.01693.

[3] V. C. Rubin, W. K. Ford Jr., and N. Thonnard. "Rotational properties of 21 SC galaxies with a large range of luminosities and radii, from NGC 4605 (R=4kpc) to UGC 2885 (R=122kpc)." In: *The Astrophysical Journal* 238 (June 1980), pp. 471–487. DOI: 10.1086/158003.

[4] J. G. de Swart, G. Bertone, and J. van Dongen. "How dark matter came to matter". In: *Nature Astronomy* 1.3 (2017). DOI: 10.1038/s41550-017-0059. URL: https://arxiv.org/abs/1703.00013.

[5] M. Lisanti. "Lectures on Dark Matter Physics". In: *New Frontiers in Fields and Strings*. WORLD SCIENTIFIC, (2016). DOI: 10.1142/9789813149441_0007. URL: https://arxiv.org/abs/1603.03797.

[6] N. Aghanim et al. "Planck 2018 results. VI. Cosmological parameters". In: *Astron. Astrophys.* 641 (2020), A6. DOI: 10.1051/0004-6361/201833910. URL: https://arxiv.org/abs/1807.06209.

[7] W. Hu. "Lecture Notes on CMB Theory: From Nucleosynthesis to Recombination". (2008). URL: https://arxiv.org/abs/0802.3688.

[8] M. Tegmark et al. "The Three-Dimensional Power Spectrum of Galaxies from the Sloan Digital Sky Survey". In: *The Astrophysical Journal* 606.2 (2004), pp. 702–740. DOI: 10.1086/382125. URL: https://arxiv.org/abs/astro-ph/0310725.

[9] A. H. Jaffe. "Cosmology 2012: Lecture Notes". Imperial College London, (2012). URL: http://www.sr.bham.ac.uk/~smcgee/ObsCosmo/Jaffe_cosmology.pdf.

[10] S. W. Allen, A. E. Evrard, and A. B. Mantz. "Cosmological Parameters from Observations of Galaxy Clusters". In: *Annual Review of Astronomy and Astrophysics* 49.1 (2011), pp. 409–470. DOI: 10.1146/annurev-astro-081710-102514. URL: https://arxiv.org/abs/1103.4829.

[11] E. van Uitert et al. "Constraints on the shapes of galaxy dark matter haloes from weak gravitational lensing". In: *Astronomy & Astrophysics* 545 (2012), A71. DOI: 10.1051/0004-6361/201219295. URL: https://arxiv.org/abs/1206.4304.

[12] L. A. Moustakas and R. B. Metcalf. "Detecting dark matter substructure spectroscopically in strong gravitational lenses". In: *Monthly Notices of the Royal Astronomical Society* 339.3 (2003), pp. 607–615. DOI: 10.1046/j.1365-8711.2003.06055.x. URL: https://arxiv.org/abs/astro-ph/0206176.

[13] R. Narayan and M. Bartelmann. "Lectures on Gravitational Lensing". (1996). URL: https://arxiv.org/abs/astro-ph/9606001.

[14] D. Clowe et al. "A Direct Empirical Proof of the Existence of Dark Matter". In: *The Astrophysical Journal* 648.2 (2006), pp. L109–L113. DOI: 10.1086/508162. URL: https://arxiv.org/abs/astro-ph/0608407.

[15] M. Milgrom. "A modification of the Newtonian dynamics as a possible alternative to the hidden mass hypothesis." In: *Astrophysical Journal* 270 (July 1983), pp. 365–370. DOI: 10.1086/161130.

[16] J. D. Bekenstein. "Relativistic gravitation theory for the modified Newtonian dynamics paradigm". In: *Phys. Rev. D* 70 (2004), p. 083509. DOI: 10.1103/PhysRevD.70.083509. URL: https://arxiv.org/abs/astro-ph/0403694.

[17] S. Tremaine and J. E. Gunn. "Dynamical Role of Light Neutral Leptons in Cosmology". In: *Phys. Rev. Lett.* 42 (1979), pp. 407–410. DOI: 10.1103/PhysRevLett.42.407. URL: https://link.aps.org/doi/10.1103/PhysRevLett.42.407.

[18] S. W. Randall et al. "Constraints on the Self-Interaction Cross Section of Dark Matter from Numerical Simulations of the Merging Galaxy Cluster 1E 0657-56". In: *The Astrophysical Journal* 679.2 (2008), pp. 1173–1180. DOI: 10.1086/587859. URL: https://arxiv.org/abs/0704.0261.

[19] P. Gondolo and G. Gelmini. "Cosmic abundances of stable particles: Improved analysis". In: *Nucl. Phys. B* 360 (1991), pp. 145–179. DOI: 10.1016/0550-3213(91)90438-4.

[20] E.W. Kolb and M.S. Turner. "The Early Universe". Frontiers in physics. *Addison-Wesley*, (1990). ISBN: 9780201116038. DOI: 10.1201/9780429492860.

[21] G. Gelmini and P. Gondolo. "DM Production Mechanisms". (2010). URL: https://arxiv.org/abs/1009.3690.

[22] G. Gelmini. "TASI 2014 Lectures: The Hunt for Dark Matter". (2015). URL: https://arxiv.org/abs/1502.01320.

[23] P. J. Fox. "TASI Lectures on WIMPs and Supersymmetry". In: *PoS* TASI2018 (2019). URL: https://inspirehep.net/files/4f24104825a24efc70195c56323c270f.

[24] M. Schumann. "Direct detection of WIMP dark matter: concepts and status". In: *Journal of Physics G: Nuclear and Particle Physics* 46.10 (2019), p. 103003. DOI: 10.1088/1361-6471/ab2ea5. URL: https://arxiv.org/abs/1903.03026.

[25] J. Cooley. "Dark Matter direct detection of classical WIMPs". In: *SciPost Physics Lecture Notes* (2022). DOI: 10.21468/scipostphyslectnotes.55. URL: https://arxiv.org/abs/2110.02359.

[26] M. W. Goodman and E. Witten. "Detectability of certain dark-matter candidates". In: *Phys. Rev. D* 31 (1985), pp. 3059–3063. DOI: 10.1103/PhysRevD.31.3059. URL: https://link.aps.org/doi/10.1103/PhysRevD.31.3059.

[27] E. Aprile et al. "Dark Matter Search Results from a One Ton-Year Exposure of XENON1T". In: *Physical Review Letters* 121.11 (2018). DOI: 10.1103/physrevlett.121.111302. URL: https://arxiv.org/abs/1805.12562.

[28] Y. Meng et al. "Dark Matter Search Results from the PandaX-4T Commissioning Run". In: *Physical Review Letters* 127.26 (2021). DOI: 10.1103/physrevlett.127.261802. URL: https://arxiv.org/abs/2107.13438.

[29] J. Aalbers et al. "First Dark Matter Search Results from the LUX-ZEPLIN (LZ) Experiment". (2022). URL: https://arxiv.org/abs/2207.03764.

[30] R. K. Leane. "Indirect Detection of Dark Matter in the Galaxy". (2020). URL: https://arxiv.org/abs/2006.00513.

[31] J. E. Gunn et al. "Some astrophysical consequences of the existence of a heavy stable neutral lepton." In: *The Astrophysical Journal* 223 (Aug. 1978), pp. 1015–1031. DOI: 10.1086/156335.

[32] M. Ackermann et al. "Searching for Dark Matter Annihilation from Milky Way Dwarf Spheroidal Galaxies with Six Years of Fermi Large Area Telescope Data". In: *Physical Review Letters* 115.23 (2015). DOI: 10.1103/physrevlett.115.231301. URL: https://doi.org/10.1103%2Fphysrevlett.115.231301.

[33] A. Acharyya et al. "Sensitivity of the Cherenkov Telescope Array to a dark matter signal from the Galactic centre". In: *Journal of Cosmology and Astroparticle Physics* 2021.01 (2021). DOI: 10.1088/1475-7516/2021/01/057. URL: https://arxiv.org/abs/2007.16129.

[34] J. L. Feng. "Dark Matter Candidates from Particle Physics and Methods of Detection". In: *Annual Review of Astronomy and Astrophysics* 48.1 (2010), pp. 495–545. DOI: 10.1146/annurev-astro-082708-101659. URL: https://arxiv.org/abs/1003.0904.

[35] O. Buchmueller, C. Doglioni, and L. Wang. "Search for dark matter at colliders". In: *Nature Physics* 13.3 (2017), pp. 217–223. DOI: 10.1038/nphys4054. URL: https://arxiv.org/abs/1912.12739.

[36] A. Boveia and C. Doglioni. "Dark Matter Searches at Colliders". In: *Annual Review of Nuclear and Particle Science* 68.1 (2018), pp. 429–459. DOI: 10.1146/annurev-nucl-101917-021008. URL: https://arxiv.org/abs/1810.12238.

[37] V. Silveira and A. Zee. "Scalar Phantoms". In: *Physics Letters B* 161.1 (1985), pp. 136–140. ISSN: 0370-2693. DOI: https://doi.org/10.1016/0370-2693(85)90624-0. URL: https://www.sciencedirect.com/science/article/pii/0370269385906240.

[38] J. McDonald. "Gauge singlet scalars as cold dark matter". In: *Physical Review D* 50.6 (1994), pp. 3637–3649. DOI: 10.1103/physrevd.50.3637. URL: https://arxiv.org/abs/hep-ph/0702143.

[39] C.P. Burgess, M. Pospelov, and T. ter Veldhuis. "The Minimal Model of nonbaryonic dark matter: a singlet scalar". In: *Nuclear Physics B* 619.1-3 (2001), pp. 709–728. DOI: 10.1016/s0550-3213(01)00513-2. URL: https://arxiv.org/abs/hep-ph/0011335.

[40] M. Ruhdorfer, E. Salvioni, and A. Weiler. "A global view of the off-shell Higgs portal". In: *SciPost Physics* 8.2 (2020). DOI: 10.21468/scipostphys.8.2.027. URL: https://arxiv.org/abs/1910.04170.

[41] R. Balkin et al. "Dark matter shifts away from direct detection". In: *Journal of Cosmology and Astroparticle Physics* 2018.11 (2018). DOI: 10.1088/1475-7516/2018/11/050. URL: https://arxiv.org/abs/1809.09106.

[42] G. Aad et al. "Observation of a new particle in the search for the Standard Model Higgs boson with the ATLAS detector at the LHC". In: *Physics Letters B* 716.1 (2012), pp. 1–29. DOI: 10.1016/j.physletb.2012.08.020. URL: https://arxiv.org/abs/1207.7214.

[43] S. Chatrchyan et al. "Observation of a new boson at a mass of 125 GeV with the CMS experiment at the LHC". In: *Physics Letters B* 716.1 (2012), pp. 30–61. DOI: 10.1016/j.physletb.2012.08.021. URL: https://arxiv.org/abs/1207.7235.

[44] "Combination of searches for invisible Higgs boson decays with the ATLAS experiment". Tech. rep. Geneva: CERN, (2020). URL: https://cds.cern.ch/record/2743055.

[45] A. Albert et al. "Searching for Dark Matter Annihilation in Recently Discovered Milky Way Satellites with Fermi-LAT". In: *The Astrophysical Journal* 834.2 (2017), p. 110. DOI: 10.3847/1538-4357/834/2/110. URL: https://arxiv.org/abs/1611.03184.

[46] H. Cheng and C. Chiang. "Revisiting scalar and pseudoscalar couplings with nucleons". In: *Journal of High Energy Physics* 2012.7 (2012). DOI: 10.1007/jhep07(2012)009. URL: https://arxiv.org/abs/1202.1292.

[47] A. Crivellin, M. Hoferichter, and M. Procura. "Accurate evaluation of hadronic uncertainties in spin-independent WIMP-nucleon scattering: Disentangling two- and three-flavor effects". In: *Physical Review D* 89.5 (2014). DOI: 10.1103/physrevd.89.054021. URL: https://arxiv.org/abs/1312.4951.

[48] G. Jungman, M. Kamionkowski, and K. Griest. "Supersymmetric dark matter". In: *Physics Reports* 267.5 (1996), pp. 195–373. ISSN: 0370-1573. DOI: https://doi.org/10.1016/0370-1573(95)00058-5. URL: https://arxiv.org/abs/hep-ph/9506380.

[49] M.A. Shifman, A.I. Vainshtein, and V.I. Zakharov. "Remarks on Higgs-boson interactions with nucleons". In: *Physics Letters B* 78.4 (1978), pp. 443–446. ISSN: 0370-2693. DOI: https://doi.org/10.1016/0370-2693(78)90481-1. URL: https://www.sciencedirect.com/science/article/pii/0370269378904811.

[50] D. Curtin and S. Gryba. "Twin Higgs portal dark matter". In: *Journal of High Energy Physics* 2021.8 (2021). DOI: 10.1007/jhep08(2021)009. URL: https://arxiv.org/abs/2101.11019.

[51] M. Frigerio et al. "Composite scalar dark matter". In: *Journal of High Energy Physics* 2012.7 (2012). DOI: 10.1007/jhep07(2012)015. URL: https://arxiv.org/abs/1204.2808.

[52] D. Marzocca and A. Urbano. "Composite dark matter and LHC interplay". In: *Journal of High Energy Physics* 2014.7 (2014). DOI: 10.1007/jhep07(2014)107. URL: https://arxiv.org/abs/1404.7419.

[53] R. Balkin et al. "Charged composite scalar dark matter". In: *Journal of High Energy Physics* 2017.11 (2017). DOI: 10.1007/jhep11(2017)094. URL: https://arxiv.org/abs/1707.07685.

[54] G. Panico and A. Wulzer. "The Composite Nambu-Goldstone Higgs". *Springer International Publishing*, 2016. DOI: 10.1007/978-3-319-22617-0. URL: https://arxiv.org/abs/1506.01961.

[55] K. Agashe and R. Contino. "Composite Higgs-mediated flavor-changing neutral current". In: *Physical Review D* 80.7 (2009). DOI: 10.1103/physrevd.80.075016. URL: https://arxiv.org/abs/0906.1542.

[56] K. Agashe, R. Contino, and A. Pomarol. "The minimal composite Higgs model". In: *Nuclear Physics B* 719.1-2 (2005), pp. 165–187. DOI: 10.1016/j.nuclphysb.2005.04.035. URL: https://arxiv.org/abs/hep-ph/0412089.

[57] B. Bellazzini, C. Csáki, and J. Serra. "Composite Higgses". In: *The European Physical Journal C* 74.5 (2014). DOI: 10.1140/epjc/s10052-014-2766-x. URL: https://arxiv.org/abs/1401.2457.

[58] R. Contino et al. "On the effect of resonances in composite Higgs phenomenology". In: *Journal of High Energy Physics* 2011.10 (2011). DOI: 10.1007/jhep10(2011)081. URL: https://arxiv.org/abs/1109.1570.

[59] S. De Curtis, M. Redi, and A. Tesi. "The 4D composite Higgs". In: *Journal of High Energy Physics* 2012.4 (2012). DOI: 10.1007/jhep04(2012)042. URL: https://arxiv.org/abs/1110.1613.

[60] N. Fonseca et al. "Dark Matter Constraints on Composite Higgs Models". (2015). URL: https://arxiv.org/abs/1501.05957.

[61] C. Grojean, O. Matsedonskyi, and G. Panico. "Light top partners and precision physics". In: *Journal of High Energy Physics* 2013.10 (2013). DOI: 10.1007/jhep10(2013)160. URL: https://arxiv.org/abs/1306.4655.

[62] D. Marzocca, A. Parolini, and M. Serone. "Supersymmetry with a pNGB Higgs and partial compositeness". In: *Journal of High Energy Physics* 2014.3 (2014). DOI: 10.1007/jhep03(2014)099. URL: https://arxiv.org/abs/1312.5664.

[63] D. Marzocca, M. Serone, and J. Shu. "General composite Higgs models". In: *Journal of High Energy Physics* 2012.8 (2012). DOI: 10.1007/jhep08(2012)013. URL: https://arxiv.org/abs/1205.0770.

[64] O. Matsedonskyi, G. Panico, and A. Wulzer. "Light top partners for a light composite Higgs". In: *Journal of High Energy Physics* 2013.1 (2013). DOI: 10.1007/jhep01(2013)164. URL: https://arxiv.org/abs/1204.6333.

[65] M. Montull et al. "Higgs couplings in composite models". In: *Physical Review D* 88.9 (2013). DOI: 10.1103/physrevd.88.095006. URL: https://arxiv.org/abs/1308.0559.

[66] G. Panico and A. Wulzer. "The discrete composite Higgs model". In: *Journal of High Energy Physics* 2011.9 (2011). DOI: 10.1007/jhep09(2011)135. URL: https://arxiv.org/abs/1106.2719.

[67] A. Pomarol and F. Riva. "The composite Higgs and light resonance connection". In: *Journal of High Energy Physics* 2012.8 (2012). DOI: 10.1007/jhep08(2012)135. URL: https://arxiv.org/abs/1205.6434.

[68] M. Redi and A. Tesi. "Implications of a light Higgs in composite models". In: *Journal of High Energy Physics* 2012.10 (2012). DOI: 10.1007/jhep10(2012)166. URL: https://arxiv.org/abs/1205.0232.

[69] R. Contino. "Tasi 2009 lectures: The Higgs as a Composite Nambu-Goldstone Boson". (2010). URL: https://arxiv.org/abs/1005.4269.

[70] B. Gripaios et al. "Beyond the minimal composite Higgs model". In: *Journal of High Energy Physics* 2009.04 (2009). DOI: 10.1088/1126-6708/2009/04/070. URL: https://arxiv.org/abs/0902.1483.

[71] G. Cacciapaglia and F. Sannino. "Fundamental composite (Goldstone) Higgs dynamics". In: *Journal of High Energy Physics* 2014.4 (2014). DOI: 10.1007/jhep04(2014)111. URL: https://arxiv.org/abs/1402.0233.

[72] D.Marzocca and A. Urbano. "Composite dark matter and LHC interplay". In: *Journal of High Energy Physics* 2014.7 (2014). DOI: 10.1007/jhep07(2014)107. URL: https://arxiv.org/abs/1404.7419.

[73] M. Kim, S. J. Lee, and A. Parolini. "WIMP Dark Matter in Composite Higgs Models and the Dilaton Portal". (2016). URL: https://arxiv.org/abs/1602.05590.

[74] C. Xing, L. Xu, and S. Zhu. "Softly shifting away from dark matter direct detection". In: *Physical Review D* 103.11 (2021). DOI: 10.1103/physrevd.103.113006. URL: https://arxiv.org/abs/2011.06264.

[75] M. Chala, G. Nardini, and I. Sobolev. "Unified explanation for dark matter and electroweak baryogenesis with direct detection and gravitational wave signatures". In: *Physical Review D* 94.5 (2016). DOI: 10.1103/physrevd.94.055006. URL: https://arxiv.org/abs/1605.08663.

[76] L. Da Rold and A. N. Rossia. "The minimal simple composite Higgs model". In: *Journal of High Energy Physics* 2019.12 (2019). DOI: 10.1007/jhep12(2019)023. URL: https://arxiv.org/abs/1904.02560.

[77] A. Ahmed, S. Najjari, and C. B. Verhaaren. "A minimal model for neutral naturalness and pseudo-Nambu-Goldstone dark matter". In: *Journal of High Energy Physics* 2020.6 (2020). DOI: 10.1007/jhep06(2020)007. URL: https://arxiv.org/abs/2003.08947.

[78] M. Ramos. "Composite dark matter phenomenology in the presence of lighter degrees of freedom". In: *Journal of High Energy Physics* 2020.7 (2020). DOI: 10.1007/jhep07(2020)128. URL: https://arxiv.org/abs/1912.11061.

[79] T. Ma and G. Cacciapaglia. "Fundamental composite 2HDM: SU(N) with 4 flavours". In: *Journal of High Energy Physics* 2016.3 (2016). DOI: 10.1007/jhep03(2016)211. URL: https://arxiv.org/abs/1508.07014.

[80] T. Ma et al. "Composite Dark Matter and Higgs". (2017). URL: https://arxiv.org/abs/1703.06903.

[81] G. Cacciapaglia et al. "Composite Higgs and Dark Matter model in SU(6)/SO(6)". In: *Journal of High Energy Physics* 2019.10 (2019). DOI: 10.1007/jhep10(2019)035. URL: https://arxiv.org/abs/1904.09301.

[82] A. Davoli et al. "Composite 2HDM with singlets: a viable dark matter scenario". In: *Journal of High Energy Physics* 2019.10 (2019). DOI: 10.1007/jhep10(2019)196. URL: https://arxiv.org/abs/1905.13244.

[83] M. Chala. "$h \to \gamma\gamma$ excess and dark matter from composite Higgs models". In: *Journal of High Energy Physics* 2013.1 (2013). DOI: 10.1007/jhep01(2013)122. URL: https://arxiv.org/abs/1210.6208.

[84] G. Ballesteros, A. Carmona, and M. Chala. "Exceptional composite dark matter". In: *The European Physical Journal C* 77.7 (2017). DOI: 10.1140/epjc/s10052-017-5040-1. URL: https://arxiv.org/abs/1704.07388.

[85] E. Bertuzzo et al. "On composite two Higgs doublet models". In: *Journal of High Energy Physics* 2013.5 (2013). DOI: 10.1007/jhep05(2013)153. URL: https://arxiv.org/abs/1206.2623.

[86] J. Barnard et al. "The unnatural composite Higgs". In: *Journal of High Energy Physics* 2015.1 (2015). DOI: 10.1007/jhep01(2015)067. URL: https://arxiv.org/abs/1409.7391.

[87] R. Nevzorov and A. W. Thomas. "E_6 inspired composite Higgs model". In: *Physical Review D* 92.7 (2015). DOI: 10.1103/physrevd.92.075007. URL: https://arxiv.org/abs/1507.02101.

[88] A. Carmona and M. Chala. "Composite Dark Sectors". 2015. URL: https://arxiv.org/abs/1504.00332.

[89] R. Balkin, G. Perez, and A. Weiler. "Little composite dark matter". In: *The European Physical Journal C* 78.2 (2018). DOI: 10.1140/epjc/s10052-018-5552-3. URL: https://arxiv.org/abs/1707.09980.

[90] T. Alanne et al. "Dark matter in (partially) composite Higgs models". In: *Journal of High Energy Physics* 2018.12 (2018). DOI: 10.1007/jhep12(2018)088. URL: https://arxiv.org/abs/1808.07515.

[91] V. Barger et al. "Complex singlet extension of the standard model". In: *Physical Review D* 79.1 (2009). DOI: 10.1103/physrevd.79.015018. URL: https://arxiv.org/abs/0811.0393.

[92] V. Barger, M. McCaskey, and G. Shaughnessy. "Complex scalar dark matter vis-à-vis CoGeNT, DAMA/LIBRA and XENON100". In: *Physical Review D* 82.3 (2010). DOI: 10.1103/physrevd.82.035019. URL: https://arxiv.org/abs/1005.3328.

[93] C. Gross, O. Lebedev, and T. Toma. "Cancellation Mechanism for Dark-Matter-Nucleon Interaction". In: *Physical Review Letters* 119.19 (2017). DOI: 10.1103/physrevlett.119.191801. URL: https://arxiv.org/abs/1708.02253.

[94] M. Gonderinger, H. Lim, and M. J. Ramsey-Musolf. "Complex scalar singlet dark matter: Vacuum stability and phenomenology". In: *Physical Review D* 86.4 (2012). DOI: 10.1103/physrevd.86.043511. URL: https://arxiv.org/abs/1202.1316.

[95] K. Huitu et al. "Probing pseudo-Goldstone dark matter at the LHC". In: *Physical Review D* 100.1 (2019). DOI: 10.1103/physrevd.100.015009. URL: https://arxiv.org/abs/1812.05952.

[96] M. Jiang et al. "Impact of a complex singlet: Electroweak baryogenesis and dark matter". In: *Physical Review D* 93.6 (2016). DOI: 10.1103/physrevd.93.065032. URL: https://arxiv.org/abs/1502.07574.

[97] C. Chiang, M. Ramsey-Musolf, and E. Senaha. "Standard Model with a Complex Scalar Singlet: Cosmological Implications and Theoretical Considerations". In: *Phys. Rev. D* 97.1 (2018), p. 015005. DOI: 10.1103/PhysRevD.97.015005. URL: https://arxiv.org/abs/1707.09960.

[98] W. Cheng and L. Bian. "From inflation to cosmological electroweak phase transition with a complex scalar singlet". In: *Phys. Rev. D* 98.2 (2018), p. 023524. DOI: 10.1103/PhysRevD.98.023524. URL: https://arxiv.org/abs/1801.00662.

[99] N. Chen et al. "Complementarity of the future e^+e^- colliders and gravitational waves in the probe of complex singlet extension to the standard model". In: *Physical Review D* 101.7 (2020). DOI: 10.1103/physrevd.101.075047. URL: https://arxiv.org/abs/1911.05579.

[100] K. Kannike and M. Raidal. "Phase transitions and gravitational wave tests of pseudo-Goldstone dark matter in the softly broken U(1) scalar singlet model". In: *Physical Review D* 99.11 (2019). DOI: 10.1103/physrevd.99.115010. URL: https://arxiv.org/abs/1901.03333.

[101] T. Alanne et al. "Pseudo-Goldstone dark matter: gravitational waves and direct-detection blind spots". In: *Journal of High Energy Physics* 2020.10 (2020). DOI: 10.1007/jhep10(2020)080. URL: https://arxiv.org/abs/2008.09605.

[102] T. Abe. "Early kinetic decoupling and a pseudo-Nambu-Goldstone dark matter model". In: *Physical Review D* 104.3 (2021). DOI: 10.1103/physrevd.104.035025. URL: https://arxiv.org/abs/2106.01956.

[103] J. M. Cline and T. Toma. "Pseudo-Goldstone dark matter confronts cosmic ray and collider anomalies". In: *Physical Review D* 100.3 (2019). DOI: 10.1103/physrevd.100.035023. URL: https://arxiv.org/abs/1906.02175.

[104] D. Azevedo et al. "One-loop contribution to dark-matter-nucleon scattering in the pseudoscalar dark matter model". In: *Journal of High Energy Physics* 2019.1 (2019). DOI: 10.1007/jhep01(2019)138. URL: https://arxiv.org/abs/1810.06105.

[105] K. Ishiwata and T. Toma. "Probing pseudo Nambu-Goldstone boson dark matter at loop level". In: *Journal of High Energy Physics* 2018.12 (2018). DOI: 10.1007/jhep12(2018)089. URL: https://arxiv.org/abs/1810.08139.

[106] S. Glaus et al. "Electroweak corrections in a pseudo Nambu-Goldstone Dark Matter model revisited". In: *Journal of High Energy Physics* 2020.12 (2020). DOI: 10.1007/jhep12(2020)034. URL: https://arxiv.org/abs/2008.12985.

[107] R. Costa et al. "Two-loop stability of a complex singlet extended standard model". In: *Physical Review D* 92.2 (2015). DOI: 10.1103/physrevd.92.025024. URL: https://arxiv.org/abs/1411.4048.

[108] S. Abe, Gi. Cho, and K. Mawatari. "Probing a degenerate-scalar scenario in a pseudoscalar dark-matter model". In: *Physical Review D* 104.3 (2021). DOI: 10.1103/physrevd.104.035023. URL: https://arxiv.org/abs/2101.04887.

[109] C. Cai, Y. Zeng, and H. Zhang. "Cancellation mechanism of dark matter direct detection in Higgs-portal and vector-portal models". In: *Journal of High Energy Physics* 2022.1 (2022). DOI: 10.1007/jhep01(2022)117. URL: https://arxiv.org/abs/2109.11499.

[110] Y. Abe, T. Toma, and K. Tsumura. "Pseudo-Nambu-Goldstone dark matter from gauged $U(1)_{B-L}$ symmetry". In: *Journal of High Energy Physics* 2020.5 (2020). DOI: 10.1007/jhep05(2020)057. URL: https://arxiv.org/abs/2001.03954.

[111] T. Abe and Y. Hamada. "A model of pseudo-Nambu-Goldstone dark matter from a softly broken $SU(2)$ global symmetry with a $U(1)$ gauge symmetry". (2022). URL: https://arxiv.org/abs/2205.11919.

[112] N. Okada and O. Seto. "Inelastic extra $U(1)$ charged scalar dark matter". In: *Physical Review D* 101.2 (2020). DOI: 10.1103/physrevd.101.023522. URL: https://arxiv.org/abs/1908.09277.

[113] D. Liu et al. "Ultraviolet completion of pseudo-Nambu-Goldstone dark matter with a hidden U(1) gauge symmetry". (2022). URL: https://arxiv.org/abs/2208.06653.

[114] Y. Abe et al. "Pseudo-Nambu-Goldstone dark matter model inspired by grand unification". In: *Physical Review D* 104.3 (2021). DOI: 10.1103/physrevd.104.035011. URL: https://arxiv.org/abs/2104.13523.

[115] N. Okada et al. "Pseudo-Goldstone dark matter in $SO(10)$". In: *Physical Review D* 104.9 (2021). DOI: 10.1103/physrevd.104.095002. URL: https://arxiv.org/abs/2105.03419.

[116] X. Jiang et al. "Pseudo-Nambu-Goldstone dark matter and two-Higgs-doublet models". In: *Physical Review D* 100.7 (2019). DOI: 10.1103/physrevd.100.075011. URL: https://arxiv.org/abs/1907.09684.

[117] H. Otsuka et al. "Pseudo-Nambu-Goldstone Dark Matter from Non-Abelian Gauge Symmetry". (2022). URL: https://arxiv.org/abs/2210.08696.

[118] N. Craig et al. "The Higgs Portal Above Threshold". In: *JHEP* 02 (2016), p. 127. DOI: 10.1007/JHEP02(2016)127. URL: https://arxiv.org/abs/1412.0258.

[119] C. Aimè et al. "Muon Collider Physics Summary". (2022). URL: https://arxiv.org/abs/2203.07256.

[120] J. De Blas et al. "The physics case of a 3 TeV muon collider stage". (2022). URL: https://arxiv.org/abs/2203.07261.

[121] S. Jindariani et al. "Promising Technologies and R&D Directions for the Future Muon Collider Detectors". (2022). URL: https://arxiv.org/abs/2203.07224.

[122] N. Bartosik et al. "Simulated Detector Performance at the Muon Collider". (2022). URL: https://arxiv.org/abs/2203.07964.

[123] J. Alwall et al. "The automated computation of tree-level and next-to-leading order differential cross sections, and their matching to parton shower simulations". In: *Journal of High Energy Physics* 2014.7 (2014). DOI: 10.1007/jhep07(2014)079. URL: https://arxiv.org/abs/1405.0301.